Journal of the European Ceramic Society 45 (2025) 117600

Contents lists available at ScienceDirect

Journal of the European Ceramic Society

journal homepage: www.elsevier.com/locate/jeurceramsoc

Composition-dependent structural, microstructural and functional characteristics of fine-grained $BaTi_{1-x}Hf_xO_3$ ceramics consolidated by Spark Plasma Sintering

Elena Mirabela Soare [a,b], Cătălina-Andreea Stanciu [b,c], Roxana Elena Pătru [d,*], Vasile-Adrian Surdu [e], Nadejda Horchidan [f,g], Liliana Mitoşeriu [f], Ioana Pintilie [d], Bogdan Ştefan Vasile [b], Adrian-Ionuţ Nicoară [b], Roxana Doina Truşcă [b], Adelina-Carmen Ianculescu [b,*]

[a] Institute of Physical Chemistry "Ilie Murgulescu", Romanian Academy, 202 Splaiul Independenței, Bucharest 060021, Romania
[b] National University of Science and Technology Politehnica Bucharest, Faculty of Chemical Engineering and Biotechnologies, Department Science & Engineering of Oxide Materials and Nanomaterials, 1-7 Gh. Polizu, Bucharest 011061, Romania
[c] National Institute for Lasers, Plasma and Radiation Physics, Atomiştilor 409, Măgurele 077125, Romania
[d] National Institute for Materials Physics, Atomiştilor 405A, Măgurele 077125, Romania
[e] Transilvania University of Braşov, Faculty of Materials Science and Engineering, Department of Materials Science, Bv. Eroilor 29, Brasov 500036, Romania
[f] Alexandru Ioan Cuza University of Iasi, Faculty of Physics, Bv Carol I 11, Iaşi 700506, Romania
[g] Alexandru Ioan Cuza University of Iasi, Institute of Interdisciplinary Research, Department of Exact and Natural Sciences, RAMTECH Center, Bv Carol I 11, Iaşi 700505, Romania

ARTICLE INFO

Keywords:
$BaTi_{1-x}Hf_xO_3$
Modified Pechini method
Spark plasma sintering
Dielectric properties
Ferroelectric behaviour

ABSTRACT

The functional properties of $BaTi_{1-x}Hf_xO_3$ ($0 \leq x \leq 0.20$) ceramics consolidated by spark plasma sintering from Pechini nanopowders are discussed in terms of the synergic effect of overlapping dissimilar structural modifications, nanoscale grain size reduction and ferroelectric-relaxor crossover. Structural and Raman investigations revealed the coexistence of various polymorph modifications. The main effects of Hf addition are: (*i*) a strong inhibiting of the grain growth process, (*ii*) the reduction of T_C and increase of the orthorhombic-tetragonal and rhombohedral-orthorhombic transition temperatures until a single, "pinched" and diffuse ferroelectric-paraelectric phase transition occurs, (*iii*) a strong flattening of the permittivity maximum, (*iv*) a slight decrease of the grain boundary resistivity, but still allowing the application of high a.c. and d.c. fields and (*v*) a gradual reduction of polarization, hysteresis loops area, energy storage capability and tunability values. Based on the dielectric and thermo-Raman results, a new low-temperature phase diagram of the fine-grained $BaTi_{1-x}Hf_xO_3$ ceramics is proposed.

1. Introduction

Ferroelectric materials exhibit a diverse range of functional characteristics that render them highly appealing for numerous applications, spanning from electronics and telecommunications to life sciences, space, and security. Due to their flexibility in accommodating a large number of elements of the periodic table, which determines versatile functional properties, the ferroelectric perovskites are among the most investigated types of electroceramics. Among them, barium titanate (BT)-based system represents the most important class of ferroelectric perovskites, due to the eco-friendly character and for specific characteristics, as high permittivity, polarization switching, PTCR (positive temperature coefficient of resistivity), piezo- and pyroelectric effects and high endurance under DC field, which make them useful for applications in electronic devices as capacitors, electromechanical transducers, thermistors, pyroelectric IR sensors, shifters, ferroelectric random access memories (Fe-RAM), nonlinear optics, etc. [1–3]. By increasing the solute content in *B*-site homovalently-substituted $BaTiO_3$

* Corresponding authors.
E-mail addresses: roxana.patru@infim.ro (R.E. Pătru), roxana.patru@infim.ro (R.D. Truşcă), adelina.ianculescu@upb.ro, a_ianculescu@yahoo.com (A.-C. Ianculescu).

https://doi.org/10.1016/j.jeurceramsoc.2025.117600
Received 16 March 2025; Received in revised form 2 June 2025; Accepted 5 June 2025
Available online 6 June 2025

ceramics with species of higher ionic radii than that one of the Ti^{4+} host cations, such as Sn^{4+} [4–12], Zr^{4+} [4,13–18], Ce^{4+} [19–22], Hf^{4+} [23–27], a few important effects are induced: (*i*) a linear decrease of the paraelectric-ferroelectric phase transition temperature, T_C (where the cubic-to-tetragonal C-T polymorph modification takes place), relative to that of $BaTiO_3$ ($T_C \sim 393$ K); (*ii*) increasingly diffuse permittivity maxima at T_C and (*iii*) a ferroelectric-relaxor crossover. Besides, unlike the *A*-site homovalent substitutions, the increase of the amount of the *B*-site solutes into BT lattice concurrently induces an opposite evolution of the low-temperature ferroelectric-ferroelectric phase transitions (*i.e.* rhombohedral-orthorhombic, R-O and orthorhombic-tetragonal, O-T) towards higher temperatures. As a result, at particular solute concentrations and temperature ranges, which are unique to each solute, distinct "pinched" phase transitions happen, where all polymorphs co-exist, marked by broadened peaks with high permittivity. Among the *B*-site solutes, Zr^{4+} and Hf^{4+} are more suitable because they possess higher chemical stability compared to Sn and Ce species, which can display different oxidation states (*i.e.* Sn^{4+}/Sn^{2+} and Ce^{4+}/Ce^{3+}) depending on the sintering conditions. Although the most similar ionic radius with one of the Ti^{4+} host ions ($r(Ti^{4+}) = 0.605$ Å) was identified for the Hf^{4+} substitute ($r(Hf^{4+}) = 0.71$ Å) [28], the functional properties of $Ba(Ti,Hf)O_3$ (BTH) ceramics have been significantly less examined compared to those of $Ba(Ti,Zr)O_3$ (BTZ) ones [4,13–18,29–34]. The first low-temperature phase diagram of the $BaTiO_3$—$BaHfO_3$ system based on structural and dielectric investigations of $BaTi_{1-x}Hf_xO_3$ (BTH) solid solutions was proposed in Ref. [35]. Further data regarding the dielectric properties were presented in Refs. [23–37], while more recent papers dealt with the study of electrocaloric effect [38,39], pyroelectric harvesting [40], piezoelectric behaviour [41], optical performance [42] and photoluminescent properties [43]. All of the mentioned studies refer to the characteristics of microstructured BTH ceramics obtained by conventional sintering of powders produced by solid-state reaction method. The compositions, the preparation parameters are summarized in Table 1.

Table 1
Compositions, preparation method and thermal parameters used to prepare microstructured $BaTi_{1-x}Hf_xO_3$ ceramics, reported in literature.

Reference	BTH compositions (mol. % Hf)	Preparation method	Thermal history	
			Calcination	*Sintering*
Payne & Tenerry [35]	0; 4; 10; 15; 20; 24; 30	Solid-state	1100°C / 2 h in air	1420°C / 1 h in air
Anwar *et al.* [23–26]	5; 10; 20; 22; 30; 40	Solid-state	1100°C / 6 h in air	1250°C / 12 h in air
Tian *et al.* [27]	3; 5; 10; 15	Solid-state	1000°C / 4 h in air	1250–1400°C / 1.5–3 h in air
Das *et al.* [36]	0; 5; 10; 15	Solid-state	950°C / 24 h in air	1300°C / 5 h in air
Garbarz-Glos *et al.* [37]	0; 1; 2.5	Solid-state	997–1327°C / 1–2 h 1350°C / 3 h in air	1397–1447°C / 1.5–3 h in air
J. Li *et al.* [38]	3; 6; 9; 10; 11; 12; 13; 15; 17; 20	Solid-state	in air	1425–1495°C / 4 h in air
M.-D. Li *et al.* [39], [40]	0; 3; 5; 8; 11; 12	Solid-state	1100°C / 2 h in air	1450°C / 5 h in air
Yin *et al.* [41]	2	Solid-state	1100°C / 2 h in air	1320, 1350, 1370, 1400°C / 4 h in air
Elorika *et al.* [42]	0; 3; 5; 8	Solid-state	2 × 1100°C / 8 h in air	1250°C / 8 h in air
Fernandez et *al.* [43]	0; 5; 10; 15	Sol-gel	1000°C / 4 h in air	1000°C / 4 h in air

The intensive development of nanotechnology involving miniaturization and integration of ferroelectrics into semiconductor technology stimulated a revival of interest in exploiting peculiar functional characteristics of nanosized or/and nanostructured BT-based systems for high performance applications [44–47]. The manufacturing of multilayer ceramic capacitors (MLCC) with high volumetric capacity requires progressively thinner dielectric layers (in the submicron range) and an increasing count of such layers. This means that these layers should consist of ceramic grains with nanometre-scale sizes, which can only be achieved when the starting oxide nanopowders, synthesized trough suitable wet-chemical processes, are consolidated using unconventional, field-assisted sintering techniques. The role of nanostructuring on the functional properties was mostly investigated in $BaTiO_3$ nanoceramics resulted by Spark Plasma Sintering (SPS) of nanopowders synthesised by innovative routes, for which some specific features have been reported, as: higher room-temperature permittivity values, lower values of the Curie temperature and Curie constant, flattened and diffuse ferroelectric-paraelectric phase transition and sometimes higher dielectric losses [48–50]. In contrast, there is a notable lack of research focused on nanocrystalline ceramics based on *A*- or *B*-site homovalently-substituted BT solid solutions. Recent works on $Ba_{1-x}Sr_xTiO_3$ [51,52], on $(Ba,Ca)(Ti,Zr)O_3$ [53] and $Bi_{0.2}K_{0.2}Ba_{0.2}Sr_{0.2}Ca_{0.2}TiO_3$ [54] SP-sintered ceramics revealed the beneficial influence of nanostructuring to increase the thermal stability of permittivity and decrease their dielectric losses, thus providing a high potential for microwave applications. Considering that in conventionally sintered BT-based ceramics, only the high homovalent substitution on B-site flatten the permittivity maximum in the Curie range, it is anticipated that the additional influence of nanostructuring will enhance the thermal stability of the dielectric response across a broader temperature range in nanocrystalline BTH ceramics compared to the coarse ones, and even with respect to the A-site substituted nanocrystalline ceramics with comparable solute content. Despite these reasonable assumptions, no papers dedicated to a systematic study of nanocrystalline BTH ceramics is found in the literature. Therefore, our work presents the synthesis and characterization of BTH nanopowders produced by the modified Pechini method and is focussed to a detailed analysis of the electrical properties of the related SP-sintered nanocrystalline ceramics, in relationship with their micro/nanostructural characteristics.

2. Experimental details

2.1. Samples preparation

The starting $BaTi_{1-x}H_xO_3$ (BTH) ($x = 0$; 0.05, 0.10 and 0.20) nanopowders were prepared by the modified Pechini method. This synthesis route produces high-purity powders, with uniform nanoparticles as shape and size and narrow particle size distribution. Moreover, the technique was selected according to the works of Li *et al.* [55,56], who indicated that this approach is the most suitable wet-chemical method for achieving constrained grain growth during the spark plasma sintering process. A similar method was also used earlier for preparing (Ba,Sr)TiO_3 nanopowders [57–59].

In the present study, beside barium carbonate ($BaCO_3$, Sigma-Aldrich 99.999 %), titanium(IV) isopropoxide ($Ti(i\text{-}OC_3H_7)_4$, Sigma-Aldrich, 97 %) and hafnium isopropoxide isopropanol adduct ($Hf(i\text{-}OC_3H_7)_4$, Sigma-Aldrich, 99.9 %) were used as raw materials, while anhydrous citric acid ($C_6H_8O_7$, Sigma-Aldrich. 99.5 %) and ethylene glycol ($C_2H_6O_2$, Sigma-Aldrich, 99.8 %) were used as chelating and esterification agents, respectively. The molar ratio of the precursors was $BaCO_3$: Ti ($i\text{-}OC_3H_7)_4$: $Hf(i\text{-}OC_3H_7)_4$: $C_6H_8O_7$: $C_2H_4O_2 = 1$: (1-x): x: 7.5: 21. (1-x)$Ti(i\text{-}OC_3H_7)_4$ and $xHf(i\text{-}OC_3H_7)_4$ in propanol were added to a clear solution of $C_6H_8O_7$ and $C_2H_6O_2$, resulted after heating at 50°C on oil bath. Thus, new, clear ($Ti_{1-x}Hf_x$) citrate solutions resulted after mixing in inert atmosphere and heating on oil bath under magnetic stirring at 80°C for 2 h. Separately, a barium citrate solution was

prepared by adding $BaCO_3$ to a $C_6H_8O_7$ 4 M solution. Further, by adding this barium citrate solution to the previously prepared ($Ti_{1-x}Hf_x$) citrate solutions, clear, transparent, yellowish Ba($Ti_{1-x}Hf_x$) solutions resulted. By heating on stove under magnetic stirring at 80°C for 1 h, these mixed solutions became increasingly viscous until yellow Ba($Ti_{1-x}Hf_x$) gels were formed. The gels were then heated on oil bath at 140°C for 36 h, in order to promote poly-condensation and to convert the gels into glassy, brown-orange resins. The Ba($Ti_{1-x}Hf_x$) resins were carefully ground and then calcined at 300°C for 3 h in static air in a vertical oven to burn off the organic matter. During this thermal treatment, the resins increase in volume, appearing as foams that represent the amorphous black precursors or the so-called "residues". After cooling, the residues, were ground to obtain glassy powders, which were then subjected to annealing in air at 900°C for 2 h, with a heating rate of 5 °C/min in order to obtain carbon-free, white $BaTi_{1-x}Hf_xO_3$ nanopowders. The as-prepared oxide powders were ultrasonically de-agglomerated and then consolidated as dense ceramic pellets of 1 cm diameter and 0.08 – 0.1 cm thickness by SPS, using a commercial equipment (FCT Systeme GmbH-Spark Plasma Sintering Furnace type HP D 1.25, Frankenblick, Germany). The applied pressure was 50 MPa, while the temperature was raised at 1050°C with a heating rate of 150 °C/min and then held at a constant value for 2 min. Rapid heating was provided by a pulsed DC current. The electric power was then switched off and the sample was cooled without pressure with a cooling rate of ~400 °C/min.

To re-oxidize the ceramics, to eliminate carbon contamination and to alleviate the associated residual stresses, a post-sintering annealing in air was performed at 850°C for 72 h, followed by a slow cooling down to the room temperature. This re-oxidizing thermal treatment completely converts some Ti^{3+} (Ti') species (formed because of the reduced atmosphere during the SPS process) into Ti^{4+}, removing the single-/doubled-ionized oxygen vacancies resulted as compensating defects for Ti'. The preparation steps of $BaTi_{1-x}Hf_xO_3$ nanopowders and related ceramics labelled as BT, BTH05, BTH10 and BTH20 are described schematically in Fig. 1.

2.2. Characterization methods

The phase composition and crystal structure of the BTH nanopowders and related SP-sintered ceramics were determined by X-ray diffraction (XRD) performed at room temperature with an Empyrean diffractometer (PANalytical, Almelo, The Netherlands) with Ni-filtered CuKα radiation (λ = 1.541874 Å), operating at 45 kV and 40 mA in θ – θ geometry. The measurements were carried out with a scan step increment of 0.026° and a counting time per step of 255 s in the 2θ range of (20 – 80)°. The XRD data were collected with a PIXCel3D detector operating in scanning-line mode. The recorded patterns were indexed using HighScorePlus 3.0.e software in conjunction with the Crystallography Open Database (COD). In order to determine structural characteristics as lattice parameters, mean crystallite size (<D>) and internal micro-strains (<S>), Rietveld refinement was carried out using a polynomial function for background approximation, a pseudo-Voigt function for peak profile, and a Caglioti function for peak width.

The nanopowders' morphology and the ceramic microstructures were examined by field-emission scanning electron microscopy (FE-SEM) with a FEI QUANTA INSPECT F50 microscope (FEI, Hillsboro, OR, US) coupled with EDX energy dispersive X-ray spectroscopy (EDX), operating at 30 kV and the nanopowders by transmission electron microscopy (TEM) and high resolution transmission electron microscopy (HR-TEM) coupled with selected area electron diffraction (SAED) with a TITAN THEMIS ultra-high resolution electron microscope (Thermo

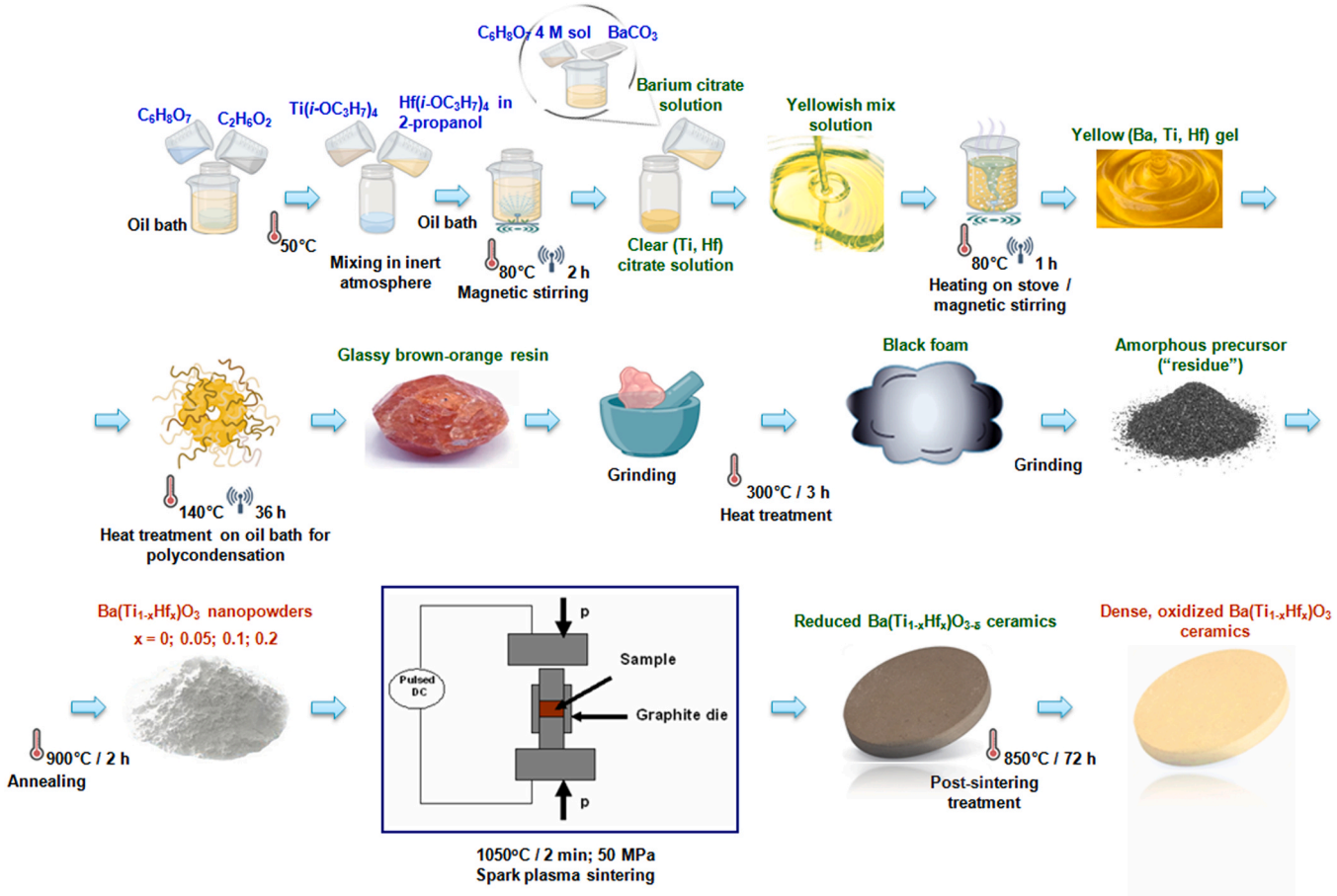

Fig. 1. Schematic representation of the processing stages for preparing $BaTi_{1-x}Hf_xO_3$ nanopowders and related dense, fine-grained ceramics.

Fisher Scientific, Waltham, MA, USA), operating at 300 kV. The average particle size, <*d*> of the BTH nanopowders and the average grain size, <*GS*> of the corresponding ceramics were estimated from the particle/grain size distributions determined with OriginPro 9.0 software (OriginLab, Northampton, MA, USA) by considering size measurements on ~100 particles/grains, using the software of the electron microscopes (ImageJ 1.50b, National Institutes of Health and the Laboratory for Optical and Computational Instrumentation, Madison, WI, USA) for SEM and Digital Micrograph 1.8.0 (Gatan, Sarasota, FL, USA) for TEM analyses. The relative densities of the SP-sintered BTH pellets were calculated as the ratio between the apparent density measured by Archimedes' method and the crystallographic (theoretical) density.

In order to perform electrical measurements, the sintered ceramic discs were polished, and their top and bottom surfaces were covered with colloidal silver paste to form stable and low-resistance electrodes, ensuring a reliable parallel-plate capacitor configuration. The complex impedance and phase shift were measured on samples in vacuum with a computer-controlled LCR Hioki 3536 impedance analyzer (Tokyo, Japan). Prior to the dielectric measurements, the impedance analyser (Hioki 3536) was calibrated by performing standard short-circuit and open-circuit corrections, in order to minimize possible parasitic contributions.

The ferroelectric $P(E)$ loops were measured at room temperature using Radiant Precision Multiferroic II Ferroelectric Test System (Radiant Technologies, INC., Albuquerque, New Mexico, USA), by using a double bipolar input with 1 Hz frequency as electric signal. The high voltage dc-tunability measurements $\varepsilon'(E)$ were performed on the electroded ceramic disks immersed in silicon oil, under high voltages produced by a High-Voltage Amplifier (TREK 30/20A-H-CE, Trek Inc., Medina, NY) coupled with a function generator (Tektronix AFG3051C) and a circuit as described in Ref. [60]. The applied field was gradually increased until the electrical response became unstable, indicating the proximity of the ceramic sample's breakdown.

The local order in fine-grained BTH ceramics was examined using Raman spectroscopy, by means of a LabRAM HR Evolution spectrometer (Horiba, Kyoto, Japan), using the 514 nm line of an argon ion laser, with a power of 125 mW, focused on spots of a few micrometers in size on the samples. Data were collected and analyzed for the non-polarized radiation scattered at 90°, with an acquisition time of 120 s during 3 runs recorded for each sample. The temperature dependence of Raman scattering was also investigated by collecting spectra recorded between 148 and 473 K, with an increment of 25 K.

3. Results and discussions

3.1. $BaTi_{1-x}Hf_xO_3$ nanopowders synthesized by the modified Pechini method

3.1.1. Phase purity and crystal structure

The room-temperature XRD patterns of $BaTi_{1-x}Hf_xO_3$ nanopowders displayed in Fig. 2(a) show the presence of the well-crystallized perovskite phase, without any detectable Ba- or Ti-rich secondary phases. Increasing hafnium proportion determines the shift of the XRD peaks towards lower values of the diffraction angle 2θ, due to the increase of the unit cell volume. This evolution and the perovskite phase's purity are clear proofs that Hf^{4+} is completely incorporated onto Ti sites in the BT lattice to create homogeneous BTH solid solutions. The crystallinity degree of all the four BTH powders exceeds 90 % (Table 2). As demonstrated by the detail of the region corresponding to the diffraction angles $2\theta = 44.5–46.5°$ in Fig. 2(b), the symmetric appearance of their profiles and the lack of any splitting of the (200) reflections seem to indicate a pseudo-cubic structure.

However, Rietveld refinement indicated that the best fits were obtained when considering a mixture of tetragonal and cubic phases for all the BTH powders under investigation (Table 2). It is important to note that, in order to fit the XRD data as accurately as possible, a number of variants were considered, taking account the complex distortions found in nanosized BT-based systems [51,61–66]. These included the single-phase model (cubic C for all the four powders, tetragonal T and orthorhombic O for BTH powders with x = 0, 0.05, 0.10 and rhombohedral R for x = 0.10, 0.20), the di-phase model (T + C for all the samples, T + R and R+C for x = 0.10 and x = 0.20), as well as tri-phase model (T + R+C for x = 0.20). It was found that T modification prevails in BT and BTH05 samples, with a slight decrease in its proportion from the undoped BT powder to the BTH05 one, while C polymorph is the major phase in BTH10 and BTH20, with a rising amount when the substitution degree increases from x = 0.10 to x = 0.20. The weighted average value of the *c/a* ratio in each di-phase sample was used to calculate the overall tetragonality. It was discovered that this parameter clearly reduces as the Hf fraction increased from x = 0 to x = 0.20. Furthermore, regardless of the type of polymorphous modification, the larger ionic radius of the Hf^{4+} compared to the host Ti^{4+} cations causes a linear increase of the lattice parameters and of the unit cell volume, as the solute content increases. Fig. 3(a) shows the evolution of the weighted average values of the unit cell volume and tetragonality *vs.* Hf

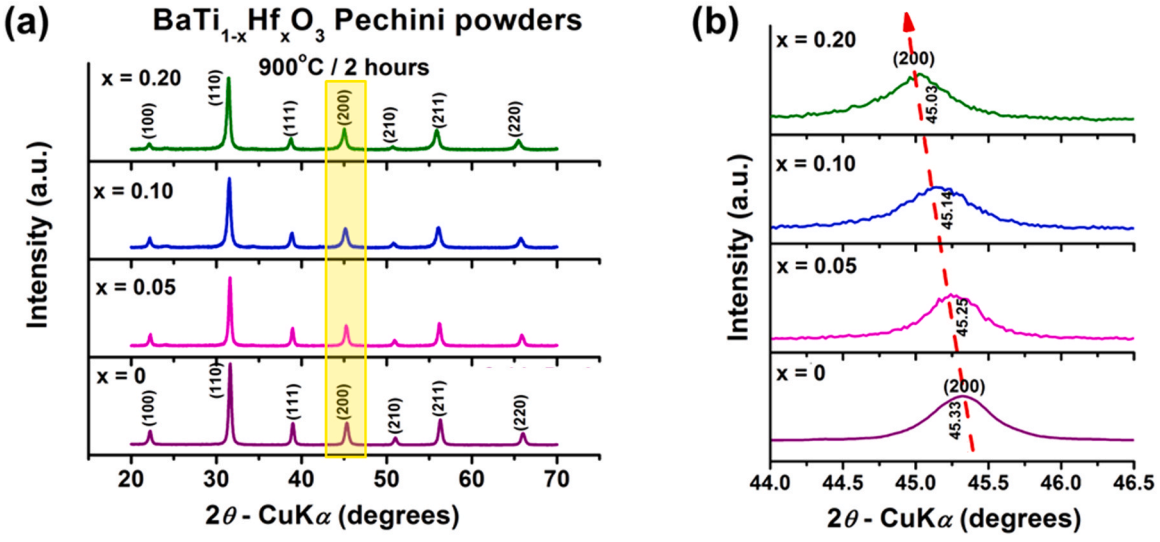

Fig. 2. (a) Room-temperature X-ray diffraction patterns of $BaTi_{1-x}Hf_xO_3$ nanopowders prepared by the modified Pechini method and annealed at 900°C for 2 h and (b) detail (the yellowish rectangle of Fig. 2(a)) of the region corresponding to the diffraction angles $2\theta = 44.5 – 46.5°$.

Table 2
Structural / morphological characteristics of the Pechini $BaTi_{1-x}Hf_xO_3$ nanopowders.

Characteristics		**Pechini $BaTi_{1-x}Hf_xO_3$ powders**							
		$BaTiO_3$		***$BaTi_{0.95}Hf_{0.05}O_3$***		***$BaTi_{0.90}Hf_{0.10}O_3$***		***$BaTi_{0.80}Hf_{0.20}O_3$***	
System		Cubic (*Pm3m*)	Tetragonal (*P4mm*)	Cubic (*Pm3m*)	Tetragonal (*P4mm*)	Cubic (*Pm3m*)	Tetragonal (*P4mm*)	Cubic (*Pm3m*)	Tetragonal (*P4mm*)
ICDD PDF4 +		04–008–2179	04–013–5892	04–008–2179	04–013–5892	04–008–2179	04–013–5892	04–008–2179	04–013–5892
Proportion (%)		31.62	68.38	37.60	62.40	61.13	38.87	69.44	30.56
Lattice parameters	***a*** **(Å)**	4.00611 ± 0.00018	3.99551 ± 0.00072	4.01281 ± 0.00022	4.00674 ± 0.00049	4.01763 ± 0.00045	4.01712 ± 0.00234	4.03200 ± 0.00064	4.05173 ± 0.00790
	b **(Å)**	4.00611 ± 0.00019	3.99551 ± 0.00072	4.01281 ± 0.00022	4.00674 ± 0.00049	4.01763 ± 0.00045	4.01712 ± 0.00232	4.03200 ± 0.00064	4.05173 ± 0.00790
	c **(Å)**	4.00611 ± 0.00018	4.02678 ± 0.00129	4.01281 ± 0.00022	4.03193 ± 0.00125	4.01763 ± 0.00045	4.05217 ± 0.00371	4.03200 ± 0.00064	4.07735 ± 0.01270
Tetragonality, *c/a*		1.0000	1.0078	1.0000	1.0063	1.0000	1.0087	1.0000	1.0063
Unit cell volume, *V* (Å^3)		64.2939	64.2840	64.6171	64.7284	64.8497	65.3907	65.5458	66.9360
Mean crystallite size, <*D*> (nm)		33.8 ± 3.1	16.9 ± 2.0	30.0 ± 3.3	15.0 ± 2.0	20.0 ± 3.1	9.0 ± 0.5	16.8 ± 3.8	5.5 ± 0.8
Micro-strains, <*S*> × 10^3		0.3 ± 0.1	0.5 ± 0.1	0.31 ± 0.09	0.6 ± 0.2	0.5 ± 0.1	1.00 ± 0.5	0.6 ± 0.2	1.8 ± 1.0
Crystallinity, (%)		97.51		90.66		98.07		92.23	
Rexp		5.53837		9.60659		9.59471		9.82113	
Rp		4.25767		5.69459		7.50708		11.73715	
Rwp		5.53763		7.41459		9.98678		15.82208	
χ^2		0.99973		0.59571		1.0834		2.5954	
Mean particle size, <d_{TEM}> (nm)		40.0 ± 10.0		28.0 ± 7.3		18.0 ± 6.1		15.3 ± 4.2	

content in BTH nanopowders.

The mean crystallite size values are lower in the T phase than those in the C one for all the BTH nanopowders. Conversely, the mean crystallite size decreases with increasing Hf content, going from 16.9 to 5.32 Å in the T phase and from 33.78 to 16.81 in the C modification. As expected, an opposite evolution *vs.* Hf content is noticed for the internal micro-strains, <*S*> (Table 2) and Fig. 3(b)).

3.1.2. Morphology

Bright-field TEM images presented in Fig. 4(a)-(d) show the morphology of the investigated BTH powders. All the compositions consist of particles with sizes in the nanometre range. Similar to the mean crystallite size, it was found that the mean particle size <*d*> dropped as the solute content increased (Fig. 3(b)), from 39.8 nm for the undoped BT powder (inset of Fig. 4(a)) down to 15.3 nm for the powder with the highest Hf content, *i.e.* BTH20 (inset of Fig. 4(d)). This trend suggests the inhibiting effect of the Hf solute on the particles coarsening. Comparing the values of the mean crystallite size calculated from the XRD data with the values of mean particle size estimated from the TEM investigations, one can conclude that the nanoparticles are predominantly single crystals. The equiaxed nanoparticles exhibit mostly polyhedral shapes with well-defined planar faces and edges and somewhat rounded corners. Some ultrafine rounded or almost spherical particles can also be noticed. Their size distributions are uni-modal, as indicated by the histograms presented as insets in the top-right corners of Fig. 4(a)-(d).

3.2. Fine-grained $BaTi_{1-x}Hf_xO_3$ ceramics consolidated by Spark Plasma Sintering

3.2.1. Phase purity and crystal structure

The XRD patterns in Fig. 5(a) for all the resulted ceramics reveal perovskite single phase structure, just like in the case of the initial BTH powders. The first detail of Fig. 5(b) corresponding to the region delimited by the light blue rectangle of Fig. 5(a) suggests a gradually change of the unit cell symmetry with the increase of Hf^{4+} addition. Thus, for the undoped BT sample, the presence of the asymmetric feature visible as a shoulder in the left side of the (200) reflection is assigned to the (002) crystalline plane, indicating a typical ferroelectric T structure (space group *P4mm*). For the BTH specimen with the lowest solute content (x = 0.05) the asymmetric profile of the (200) reflection is preserved, but with a modification of the intensity ratio of the two adjacent (002)/(200) peaks. Unlike the undoped sample, where the intensity of (200) reflection prevails over the low-intensity (002) reflection, in the BTH05 specimen an opposite ratio is noticed. This feature is specific to the O structure (space group *Amm2*), where the first peak marked by an asterisk-type symbol in Fig. 5(b) is assigned to the (022) crystalline plane. This ratio is ~1.18 for the BTH05 ceramic, which represents an intermediate value between that one corresponding to the I_{002} / I_{200} ratio of 0.52, specific to the tetragonal phase (ICDD file no. 01–084–9614), and that of 2.00 (ICDD file no. 01–090–2459), corresponding to a pure O phase. This suggests that in this composition, a mixture of T + O phases, with a slight predominance of the O modification, should be considered. This finding is supported by analyzing the second detail of Fig. 5(c), which corresponds to the region of $2\theta = 73 - 76.5^{\circ}$, delimited by the pink rectangle in Fig. 5(a). The structural modification, as the Hf content increases from x = 0 to x = 0.05 is emphasized by the splitting of the (301)/(310) peak, specific to the T $BaTiO_3$ in two adjacent peaks, *i.e.* (042)/(113) and (331), which correspond to the O distortion. These peaks together with the (024) reflection of the O structure which corresponds to the (103) reflection in the T polymorph are slightly shifted to lower diffraction angles. Therefore, one can conclude that at room temperature, BTH05 composition should be placed in the proximity of the O-T phase transition.

The presence of similar double-phase (O+T) mixture in $BaTi_{1-x}M_xO_3$ (M = Hf, Zr, Sn) compositions with $0.2 \leq x \leq 0.5$ was earlier reported by

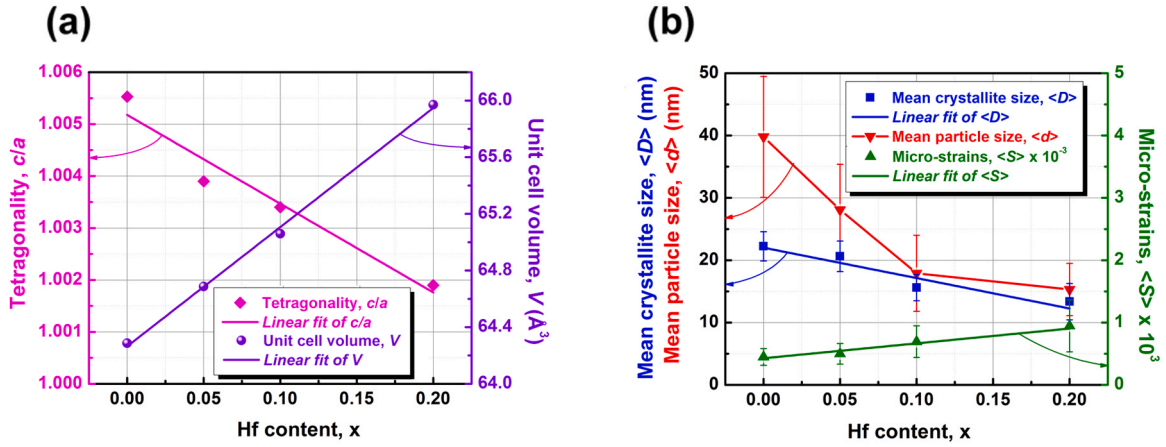

Fig. 3. Dependence of the structural / morphological parameters on Hf content in BTH nanopowders: (a) the weighted average of both the tetragonality degree, c/a and the unit cell volume, V and (b) the weighted average of the mean crystallite size, $<D>$, as well as of the internal micro-strains $<S>$ and mean particle size $<d>$.

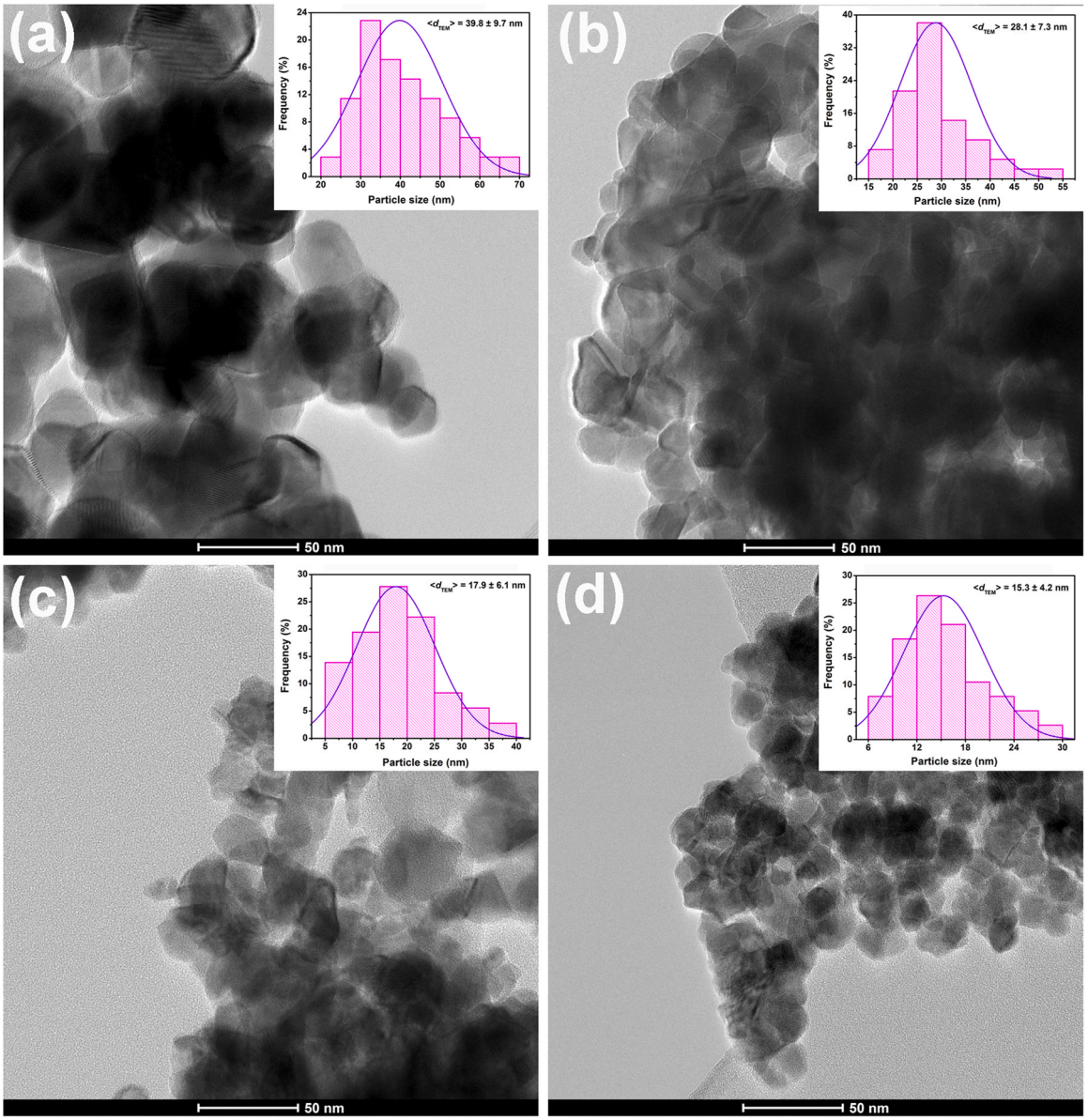

Fig. 4. (a)-(d) TEM images of the $BaTi_{1-x}Hf_xO_3$ nanopowders prepared by the modified Pechini method and annealed at 900°C for 2 h: (a) x = 0; (b) x = 0.05; (c) x = 0.10 and (d) x = 0.20; the insets in the top-right corners of (a)-(d) display the histograms indicating the particle size distributions for the investigated powders.

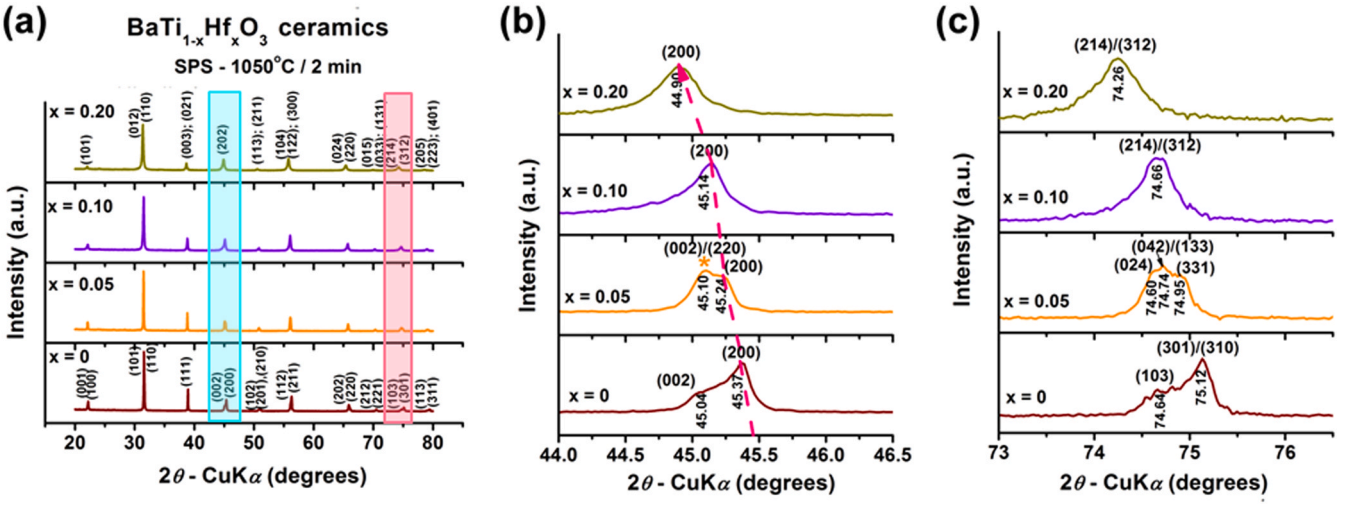

Fig. 5. (a) Room-temperature X-ray diffraction patterns of $BaTi_{1-x}Hf_xO_3$ ceramics consolidated by SPS at 1050°C for 2 min; (b) detail (the light blue rectangle of Fig. 5(a)) of the region corresponding to the diffraction angles $2\theta = 44.5 - 46.5°$ and (c) detail (the pink rectangle of Fig. 5(a)) of the region corresponding to the diffraction angles $2\theta = 73 - 76.5°$.

several research groups [38–40,42,67,68]. A further increase of Hf content causes a new structural change, so that for the BTH10 and BTH20 ceramics a single peak was only detected, as shown in both detail images of Fig. 5(b) and (c). This suggests the presence of a single-phase ceramic with either a C or a T structure, or a double-phase composition consisting of a mixture of the two (R+C) phases.

Using Rietveld refinement, the best fits were obtained by considering a T structure for BT and BTH05 ceramics and a mixture of R (space group *R3m*) and C (space group *Pm3m*) phases in BTH10 and BTH20 samples (Table 3).

The profiles of the BTH05 ceramic's most structurally-change-sensitive diffraction peaks were analysed, and the results showed that the ICDD files of the O structure did not fit well the diffraction data. This is not surprising, considering that earlier studies [10,69] have indicated that the coherence length of XRD, which averages over more than 10^4 unit cells, is insufficient to accurately identify small local distortions and distinguish clearly between the T and O modifications in substituted BT-based ceramics through the related refinement process. Additional electrical measurements depending on temperature and Raman spectroscopy studies are necessary to enhance the understanding of the structural changes in the BTH solid solutions. The R modification prevails in BTH10 and BTH20 specimens, but its proportion reduces; consequently, the proportion of the C phase increases, as the solute content increases. The structural analysis indicates that BTH20 sample is in the proximity of the ferroelectric-paraelectric phase transition at room temperature.

The influence of Hf content on the structural parameters, specifically rising both the unit cell volume and the internal micro-strains while reducing the average crystallite size as the solute content increases, is similar to that acting in the starting BTH powders.

3.2.2. Microstructure and chemical composition

The FE-SEM image of the BT fresh fractured ceramic shows a dense, homogeneous, fine-grained microstructure, consisting of well-faceted polyhedral grains, uniform as shape and size (Fig. 6), which by strongly-welding generated almost perfect triple junctions. The pore-free sample exhibits a relative density of 99.4 % and uni-modal grain size distribution, with an average grain size, $<GS>$ of 0.97 μm (Table 4 and inset of Fig. 6(a)).

Incorporation of 5 mol.% Hf on Ti sites in BTH05 specimen induces specific disruption in the microstructure, resulting from the early fragmentation of the ceramic grains (Fig. 6(b)). This process affects the overall microstructural uniformity and causes the appearance of a small fraction of intergranular porosity, which causes the slight decrease of the relative density to 97.7 % (Table 4). The average grain size decreases to 0.76 μm (Table 4) and the grain size distribution becomes broader than one corresponding to the undoped BT sample, showing an incipient tendency toward a bi-modal type, with a major fraction (~58 %) of smaller grains, with sizes below 0.6 μm, and about ~12 % larger grains, with sizes ranged between (1.5 − 1.8) μm (inset of Fig. 6(b)).

The increase of the hafnium content in BTH10 and BTH20 ceramics has a remarkable effect on the grain size, which strongly decreases toward the nanometre range (Fig. 6(c) and (d)). Thus, $<GS>$ values of 69 and 57 nm, were estimated for BTH10 and BTH20, respectively (Table 4). The drop in the grain size is much steeper than one of the particle size in the starting BTH powders.

Despite their small size, the polyhedral shape and the faceting of the ceramic grains is maintained, as reveal by the insets shown in Figs. 6(c) and 6(d). Microstructural uniformity and densification are restored, while the uni-modal grain size distributions become narrower, as indicate the histograms of the insets of the mentioned figures. These results are in agreement with those reported for solid-state prepared BTH ceramics in Ref. [42], where the minimum porosity was reached for the undoped sample, while the maximum one was found in the $BaHf_{0.05}Ti_{0.95}O_3$ specimen. Relative density values of 98.8 and 98.5 % were reached for BTH10 and BTH20 ceramics, respectively.

An indication of chemical purity in all the investigated BTH ceramics is also provided by the EDX spectroscopy. Thus, in the corresponding EDX spectra, only species belonging to the perovskite BTH phases, *i.e.* Ba, Ti, Hf and O were detected (Fig. 7(a)). The evolution of the characteristic Hf peaks, whose intensities are gradually enhanced as the Hf content increases, is shown in the detail of Fig. 7(b).

3.2.3. Low-field dielectric properties

3.2.3.1. Dielectric properties vs. temperature. Fig. 8(a)-(d) presents the temperature dependence of real part of permittivity (ε') and dielectric losses ($\tan\delta$), for a few selected frequencies in the ($10^2 - 10^6$) Hz range.

Fig. 8(a) shows a typical behaviour for barium titanate ceramics, with a significant increase in permittivity with temperature, reaching at 1 kHz frequency a prominent maximum of 6113 at 385 K, despite the small grain size of the ceramic sample. This peak corresponds to the ferroelectric-to-paraelectric phase transition (T-C). Additionally, a broad shoulder around ~290 K indicates the O-T phase transition, while a less prominent feature near 205 K marks the R-O one. The permittivity

Table 3
Structural parameters of the SP-sintered $BaTi_{1-x}Hf_xO_3$ ceramics.

Characteristics		SP-sintered $BaTi_{1-x}Hf_xO_3$ ceramics				
		BaTiO₃	***BaTi$_{0.95}$Hf$_{0.05}$O₃***	***BaTi$_{0.90}$Hf$_{0.10}$O₃***		***BaTi$_{0.80}$Hf$_{0.20}$O₃***
System		Tetragonal (*P4mm*); Z = 1	Tetragonal (*P4mm*); Z = 1	Rhombohedral / Hexagonal (*R3m*); Z = 3	Cubic (*Pm3m*); Z = 1	Rhombohedral / Hexagonal (*R3m*); Z = 3	Cubic (*Pm3m*); Z = 1
ICDD PDF4 +		01–084–9614	01–084–9614	01–085–0368	01–085–9614	01–085–0368	01–085–9614
Proportion (%)		100	100	67.79	32.21	59.07	40.93
Lattice parameters	***a*** **(Å)**	3.99596 ± 0.00012	4.00774 ± 0.00012	5.68150 ± 0.00239	4.02948 ± 0.00097	5.70899 ± 0.0080	4.049 ± 0.00183
	b **(Å)**	3.99596 ± 0.00012	4.00774 ± 0.00012	5.68150 ± 0.00239	4.02948 ± 0.00097	5.70899 ± 0.0080	4.049 ± 0.00183
	c **(Å)**	4.01634 ± 0.00015	4.02023 ± 0.00015	6.95599 ± 0.00577	4.02948 ± 0.00097	6.99053 ± 0.01942	4.049 ± 0.00183
	α **(°)**	90	90	90	90	90	90
	β **(°)**	90	90	90	90	90	90
	γ **(°)**	90	90	120	90	120	90
Unit cell distortion, *c/a*		1.0051	1.0031	1.2243	1.0000	1.2245	1.0000
Unit cell volume, *V* (Å^3)		64.1317	64.5727	194.4538	65.4255	197.2147	66.3811
Average crystallite size, <*D*> (nm)		71.0 ± 39.3	64.0 ± 33.3	43.1 ± 12.1	23.0 ± 12.0	28.0 ± 8.5	11.0 ± 2.1
Micro-strains, <*S*> × 10^3		0.14 ± 0.03	0.15 ± 0.02	0.31 ± 0.61	0.48 ± 0.18	0.32 ± 0.06	0.97 ± 0.57
R_{exp}		7.36066	7.54559	7.05852		6.91576	
R_p		6.16706	6.40304	7.2381		8.93896	
R_{wp}		9.09108	9.23061	10.89085		13.85038	
χ^2		1.52545	1.49649	2.38065		4.01091	

slightly decreases with increasing frequency, indicating the presence of dipolar relaxation, caused by the inability of dipolar entities to follow the rapidly alternating electric field at higher frequencies. The smaller grain size and high densification achieved through SPS may contribute to both the increased dielectric losses and the stability of the permittivity at higher frequencies. The dielectric losses tan δ remains below 0.15 throughout the investigated temperature and frequency ranges. Both the permittivity $\varepsilon'(T)$ and the dielectric losses tan $\delta(T)$ indicate no significant contributions from conduction processes.

The behaviour of tan $\delta(T)$ reflects the structural and energetic changes associated with the phase transitions observed in $\varepsilon'(T)$. No increase in losses at higher temperatures, which may be attributed to thermally activated processes related to ionic or electronic conduction, is observed in the paraelectric (cubic) phase of BT. Relaxation associated with dipolar polarization is confirmed by the sharper increase of tan $\delta(T)$ in the proximity of the phase transition regions identified in $\varepsilon'(T)$. The stability of losses in the cubic phase suggests that conduction-related mechanisms do not dominate, reinforcing the idea that dielectric response in this region remains primarily governed by intrinsic dipolar dynamics rather than extrinsic contributions such as interfacial polarization or Maxwell-Wagner-type effects.

The addition of 5 mol.% Hf (x = 0.05) to BT determines a decrease in the permittivity peak from 6113 at 385 K (undoped BT) to 3560 at 380 K (Fig. 8(b)). The slight shift in the peak temperature suggests that the ferroelectric-to-paraelectric phase transition (T-C) is moderately affected by the Hf incorporation. The O-T transition (~315 K) and the R-O one (~260 K), become less pronounced upon Hf addition compared to undoped BT. This attenuation indicates a reduction in the energy differences between these phases. The dielectric loss tan $\delta(T)$ remains relatively low (tan $\delta = 0.15$) over the entire temperature and frequency investigated range, indicating that a low degree of Hf content does not introduce significant conduction contributions.

The increase of Hf amount in BTH10 results in a drop of the real part of permittivity and a further shift in the Curie temperature toward lower temperature values (Fig. 8(c)). The maximum permittivity decreases to ~2060 at 340 K, compared to BT and BTH05 specimens. The lowering of the Curie temperature from 385 K (undoped BT) and 380 K (BTH05) down to 340 K in BTH10 highlights the stronger influence of high Hf content on the ferroelectric-to-paraelectric (T-C) phase transition. This drop of the ferroelectric-paraelectric phase transition temperature can be associated with the synergic role of Hf addition combined with the severe decrease of the grain size toward the nanometre range, as the solute content increases from x = 0.05 to x = 0.10.

A reduction of Curie temperature when reducing grain size at nanoscale has been usually reported for undoped nanocrystalline $BaTiO_3$ ceramics [47–50]. The O-T transition (normally observed near ~290 K in undoped BT and ~315 K in BTH05) and the R-O transition (visible at ~205 K in undoped BT and ~260 K in BTH05) become indistinguishable in BTH10. This indicates a further reduction in the energy differences between the ferroelectric phases. The so-called "pinched transition" defined by a single, broadened permittivity maximum that occurs above a certain solute proportion in homovalent *B*-site $BaTiO_3$ solid solutions, arises from the contrasting temperature-dependent behaviours of the ferroelectric-to-paraelectric phase transition and of the low-temperature O-T and R-O polymorph transformations transitions. This phenomenon was clearly noticed in both BTH10 and BTH20 samples.

A similar solute proportion inducing the occurrence of the "pinched phase transition" was previously reported also for BTZ ceramics [33]. Nonetheless, the notably reduced temperature associated with the "pinched phase transition" (T_m = 340 K) identified for BTH10 in this study compared to the 355 K (82°C) observed for BTZ10 [33] can be accounted for the influence of increased internal stress caused by nanostructuring. Microstrains favour faster decrease of ferroelectric-paraelectric transition temperature, T_m, concurrently with a more pronounced increase of both the O-T and R-O transition

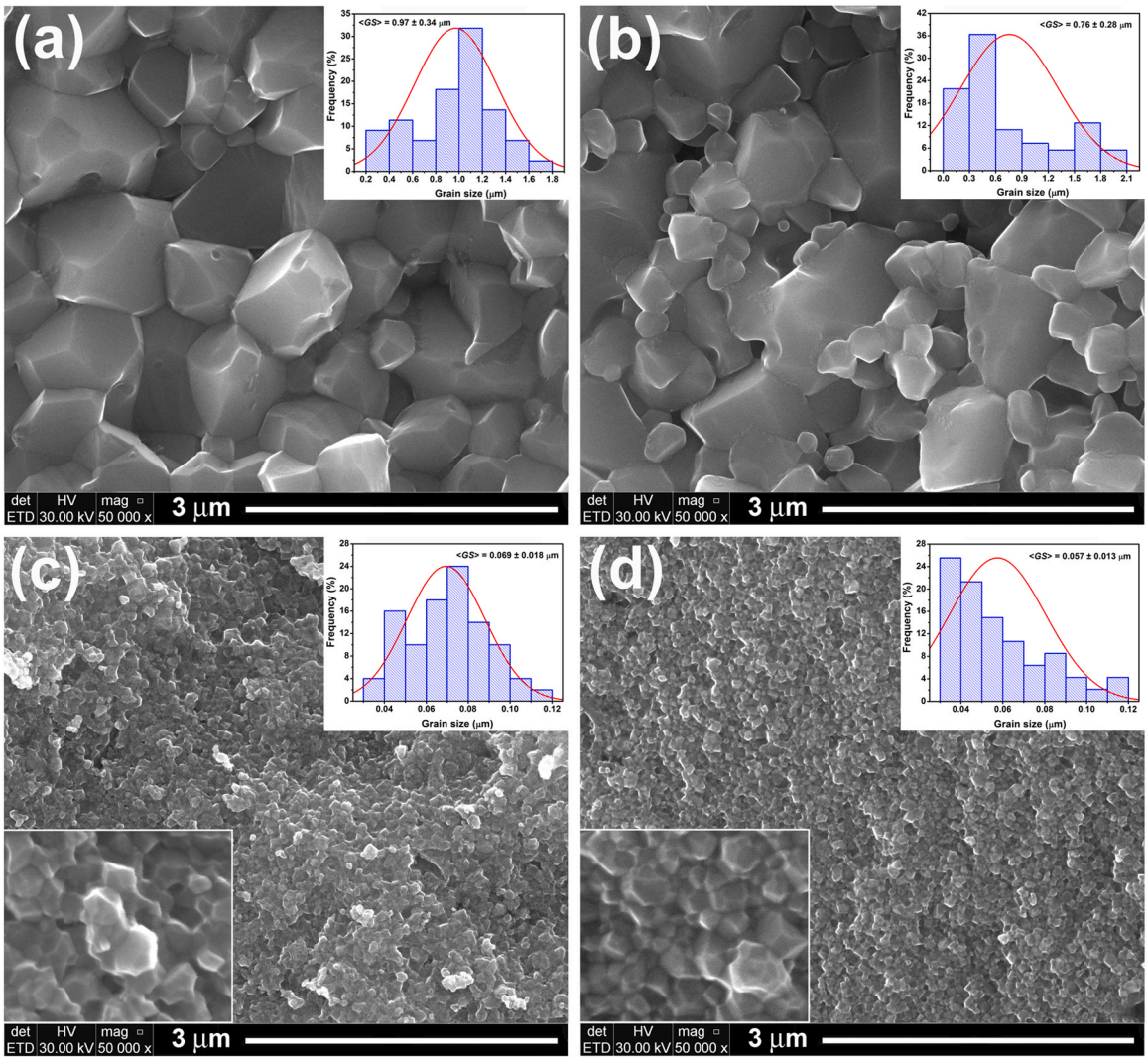

Fig. 6. (a)-(d) FE-SEM images in fracture of the $BaTi_{1-x}Hf_xO_3$ ceramics derived from the Pechini nanopowders and consolidated by SPS at 1050°C / 2 min: (a) x = 0; (b) x = 0.05; (c) x = 0.10 and (d) x = 0.20; the insets in the top-right corners of (a)-(d) display the histograms indicating the grain size distributions for all the ceramics under investigation; the insets in the bottom-left corners of Fig. 5(c) and (d) show details of the microstructure of the nanocrystalline $BaTi_{0.90}Hf_{0.10}O_3$ and $BaTi_{0.80}Hf_{0.20}O_3$ ceramics, respectively.

temperatures (T_1 and T_2) compared to the microstructured ceramics of similar compositions.

The dielectric losses decrease almost linearly as the temperature increases, tan $\delta(T)$ reaching values below 15 % over the entire investigated temperature range. However, for frequencies below 200 kHz, the dielectric losses exhibit values below 6 % in the temperature range of (150 − 470) K.

Further increase of the solute content (x = 0.20) leads to a substantial reduction in the permittivity and a further lowering of the Curie temperature in the BTH20 sample (Fig. 8(d)). The maximum permittivity decreases to ~812 at 275 K, marking a significant decline compared to the undoped BT sample, as well as to the ceramics with lower Hf content, *i.e.* BTH05 and BTH10. As in the case of BTH10 specimen, the polymorphic T-O and O-R transitions are no longer distinguishable in BTH20. This feature, along with the strong flattening of the permittivity maximum indicates a near-complete suppression of the long-range ferroelectric order, consistent with: (*i*) the increased structural disorder and stronger dilution of dipolar interactions caused by higher Hf substitution degrees and (*ii*) the reticular disruption induced by nanostructuring. The notable decrease in the maximum permittivity and the rise in the diffuseness of the ferroelectric-paraelectric phase transition with higher Hf content indicate intensified relaxation processes, signifying the transition from a long-range ferroelectric order to a behaviour dominated by local polarization effects. Besides, the slight shift of the permittivity maximum toward higher temperatures with rising frequency, along with the increasingly high frequency dispersion of the permittivity below T_C as the Hf content increases from x = 0.10 to x = 0.20 suggests a gradual evolution to a relaxor-like state. For BTH20, the dielectric losses, expressed as tan $\delta(T)$ remain reduced (below 5 %) in the temperature range of (150 − 470) K, for frequency values below 200 kHz.

The temperature dependence of the real part of permittivity for the undoped BT and for the BTH ceramics is plotted in Fig. 9(a) at 1 kHz for the Curie – Weiss analysis, together with tan $\delta(T)$ (Fig. 9(b)) to better compare the influence of Hf solute on the dielectric behaviour. At room temperature, the permittivity (ε'_{RT}) values decrease form 3404 for undoped BT to 2174 for BTH05, further to 1922 for BTH10 and down to 808 for BTH20 (Table 5). At 1 kHz, the dielectric losses show values below 6.3 % over the entire investigated temperature range. These are considered usual values for $BaTiO_3$-based ferroelectric ceramics. At room temperature, the $(\tan \delta)_{RT}$ values decrease monotonically from 0.03 for undoped BT to 0.022 for BTH05, then to 0.015 for BTH10 and, finally, to 0.013 for BTH20 sample (Table 5), revealing the favourable effect of the Hf solute on the dielectric character of these compositions.

Table 4
Microstructural parameters of the SP-sintered $BaTi_{1-x}Hf_xO_3$ ceramics.

Microstructural characteristics	**SP-sintered $BaTi_{1-x}Hf_xO_3$ ceramics**			
	BaTiO₃	***$BaTi_{0.95}Hf_{0.05}O_3$***	***$BaTi_{0.90}Hf_{0.10}O_3$***	***$BaTi_{0.80}Hf_{0.20}O_3$***
Average grain size, <*GS*> (μm)	0.97 ± 0.34	0.76 ± 0.28	0.069 ± 0.018	0.057 ± 0.013
Grain size distribution and microstructural uniformity	◆ broad; ◆ symmetric unimodal, with grains sizes of (0.2 – 1.8) μm; ◆ uniform.	◆ broad; ◆ unimodal, asymmetric to left side, with an incipient tendency towards bimodal: - major fraction (~58 %) of smaller grains, with sizes < 0.6 μm - minor fraction (~12 %) of larger grains, with sizes of (1.5 – 1.8) μm; ◆ non-uniform.	◆ narrow; ◆ unimodal, symmetric, with grains sizes of (0.03 – 0.12) μm; ◆ uniform.	◆ narrow; ◆ unimodal, asymmetric to left side, with grains sizes of (0.03 – 0.12) μm; ◆ uniform.
Type of porosity	residual intragranular	intergranular	intergranular	intergranular
Apparent density, ρ_a (g/cm^3)	6.00	6.02	6.20	6.42
Relative density, ρ_r (%)	99.4	97.7	98.8	98.5
Porosity, *P* (%)	0.6	2.3	1.2	1.5

Fig. 9(a) highlights the systematic changes of the dielectric behaviour with increasing Hf concentration: permittivity reduction, suppression of ferroelectric phase transitions and Curie temperature reduction with a rate of 5.5 K/at% as the Hf content increased from x = 0 to x = 0.20. The permittivity of typical ferroelectrics obeys the Curie–Weiss law in the paraelectric phase above the Curie temperature T_C [70]. Increasing Hf content along with grain size reduction leads to a higher degree of diffuseness of the ferroelectric-paraelectric phase transition. The nature of the dispersion and the degree of the diffuseness was analyzed by using the modified Curie-Weiss equation (Fig. 9(a)) [71]:

$$\frac{\varepsilon'_A}{\varepsilon} = 1 + \frac{(T - T_A)^\gamma}{2\delta^2}, \quad (1)$$

in which ε'_A is the maximum permittivity at the corresponding temperature T_A, δ describes the temperature range over which the phase transition occurs, and γ is the diffuseness degree of the phase transition ($1 \leq \gamma \leq 2$, $\gamma = 1$ for typical ferroelectrics and $\gamma = 2$ for "full relaxor state"). The parameters ε'_A and T_A are determined by fitting the dielectric data with the Lorentzian Eq. (1) and are compared with the maximum permittivity ε'_m at its corresponding T_C. While ε'_A may differ slightly from the measured ε'_m, T_A is found to be close to T_C. The significant reduction in both ε'_A and ε'_m reflect the suppression of long-range ferroelectric order due to Hf doping, while the drop of T_A and T_C indicates the destabilization of the ferroelectric state caused by Hf-induced lattice distortions. The fitting parameters along with experimental data are listed in Table 5.

The parameter δ increases with the increase of Hf content. The sharp phase transition observed in undoped BT becomes slightly broadened for BTH05, moderately diffuse for BTH10, and highly diffuse for BTH20. Similarly, the parameter γ also increases with Hf addition, indicating a progressive shift from the sharp ferroelectric transition specific to BT to the onset of diffuse behaviour for BTH05, a moderate diffuse phase transition for BTH10 and almost a relaxor-like behaviour for BTH20. The increase in both δ and γ suggests that the material approaches a ferroelectric-relaxor crossover at higher Hf concentrations, where the phase transition is dominated by localized nanopolar clusters rather than long-range ferroelectric domains. This behaviour is characteristic of materials with significant structural disorder and the effect is enhanced by the grain size reduction in nanoscale range.

The introduction of Hf solute on Ti sites into the BT lattice generates local distortions that disrupt the long-range ferroelectric order, leading to localized polarization effects and a broader temperature range for the phase transition. The increasing broadening of the ferroelectric-paraelectric phase transition observed at higher Hf content ($0.10 \leq x \leq 0.20$) are primarily attributed to the more significant structural disorder and hence to the dilution of dipolar polarization caused by the substitution of Ti^{4+} with Hf^{4+} in the $[TiO_6]$ octahedral framework. At higher Hf concentrations, the distortions become more pronounced, creating short-range polar regions, that weakly interact each other. This behaviour is responsible for the diffuse phase transitions and lower permittivity values observed experimentally. Furthermore, the significant lattice distortions enhance localized charge-trapping mechanisms, resulting in additional polarization relaxation processes. These effects are evident in the broader and more flattened dielectric response curves. The attenuation of ferroelectric transitions reflects a substantial disruption of ferroelectric order, consistent with increased structural disorder and a weakening of long-range dipolar interactions. The nanostructure seems to play a key-role in diluting the ferroelectric character due to the high density of grain boundary regions, where the significant rise of the related micro-strains could induce a structural heterogeneity of the ceramic grains. Therefore, in BTH10 and BTH20, the presence of the so-called "composite" grains, consisting of non-polar dead-layers and cores with a longer- or shorter-range polar ordering, as those reported for nanocrystalline (Ba,Sr)TiO_3 ceramics [51], [52],

cannot be excluded.

It is worth to mention that the values of the ferroelectric-paraelectric transition temperature T_C / T_m for our BTH samples are slightly lower as a result of the smaller grain sizes than those reported by most of the recent papers, who investigated coarser ceramics with similar compositions, but prepared by the classical solid-state reaction method (Fig. 10) [27,35,38–40,42].

3.2.3.2. Dielectric properties vs. frequency. To complete the temperature-dependent dielectric analysis, frequency-dependent real (ε') and imaginary (ε'') parts of permittivity and loss tangent (tan δ) were investigated at two fixed temperatures representative of the ferroelectric and paraelectric phases. The selected temperatures were 250 K ($T < T_C$), corresponding to the ferroelectric phase, and 425 K ($T > T_C$), within the paraelectric region. This approach allows for a more detailed examination of how hafnium solute influences the dielectric response over a wide frequency range (10^2 – 10^6 Hz).

Undoped BT exhibits the highest permittivity values, with a weak frequency dependence up to ~10^5 Hz at high temperatures ($T > T_C$), followed by a slight increase at higher frequencies (Fig. 11(a)). This increase suggests the presence of interfacial polarization effects, which may stem from charge accumulation at grain boundaries. Hafnium doping systematically reduces ε' across all frequencies, indicating a suppression of long-range ferroelectric interactions and a stabilization of the paraelectric phase. In contrast, at low temperatures ($T < T_C$), all compositions exhibit a slight decrease in permittivity with increasing frequency, characteristic of dipolar relaxation mechanisms (Fig. 11(b)). The decay is more pronounced in undoped BT, whereas the doped BTH compositions exhibit a more stable $\varepsilon'(f)$ response, suggesting reduced polarization dynamics and a diminished contribution from domain wall motion. The almost invariant $\varepsilon'(f)$ dependence curve for the specimen with the highest Hf content (BTH20) further supports the idea of short-range polar ordering instead of classical long-range ferroelectricity.

The frequency dependence of imaginary permittivity ε'' provides insight into the dissipation mechanisms (Fig. 11(c), (d)). At $T > T_C$, ε'' decreases at intermediate frequencies and rises sharply beyond ~10^5 Hz in undoped BT. This behaviour is commonly associated with nearest-neighbour hopping or highly localized charge motion at high frequencies, according to Funke's criteria [72] (Fig. 11(c)). Hafnium addition progressively suppresses this high-frequency conduction contribution, suggesting that Hf incorporation enhances the structural disorder and localizes charge carriers, thereby reducing long-range charge transport.

At $T < T_C$, the imaginary permittivity ε'' of undoped BT exhibits a peak at intermediate frequencies (~10^2 – 10^4 Hz), and a less pronounced variation with frequency in the doped BTH compositions (Fig. 11(d)), suggesting that the polarization mechanisms become more localized with increasing Hf content. The overall reduction in ε'' in the whole frequency range in BTH20 reinforces the transition toward a relaxor-like state, where polarization dynamics are governed by local fluctuations rather than collective domain interactions. The material exhibits a weaker dielectric response due to the suppression of long-range interactions, consistent with the earlier observation of a diffuse phase transition.

Moreover, the different trends observed between the low-frequency (10^2 Hz – 10^3 Hz) and middle-frequency (10^4 Hz – 10^5 Hz) regions in the ε'' (f) behaviour may suggest the involvement of multiple relaxation mechanisms. In particular, oxygen vacancy-related relaxations cannot be entirely ruled out and could have a minor contribution to the observed behaviour, as previously reported for $BaTiO_3$-based ceramics [42,73].

The frequency dependence of the dielectric losses (tan δ) shown in Fig. 11(e) for the paraelectric state ($T > T_C$, 425 K) and in Fig. 11(f) for the ferroelectric state ($T < T_C$, 250 K) provides further evidence of relaxation processes and insights into the dissipation mechanisms and polarization stability in both phases. For the paraelectric state, in the low-frequency range, below 10^5 Hz, BTH20 ceramic exhibits the highest initial tan δ value, indicating that the hafnium content influences the energy dissipation mechanisms in this region. BT maintains the lowest losses across this range, similar to BTH10, suggesting that the lack of solute or a moderate Hf content stabilizes the dielectric response by reducing extrinsic contribution such as interfacial polarization effects.

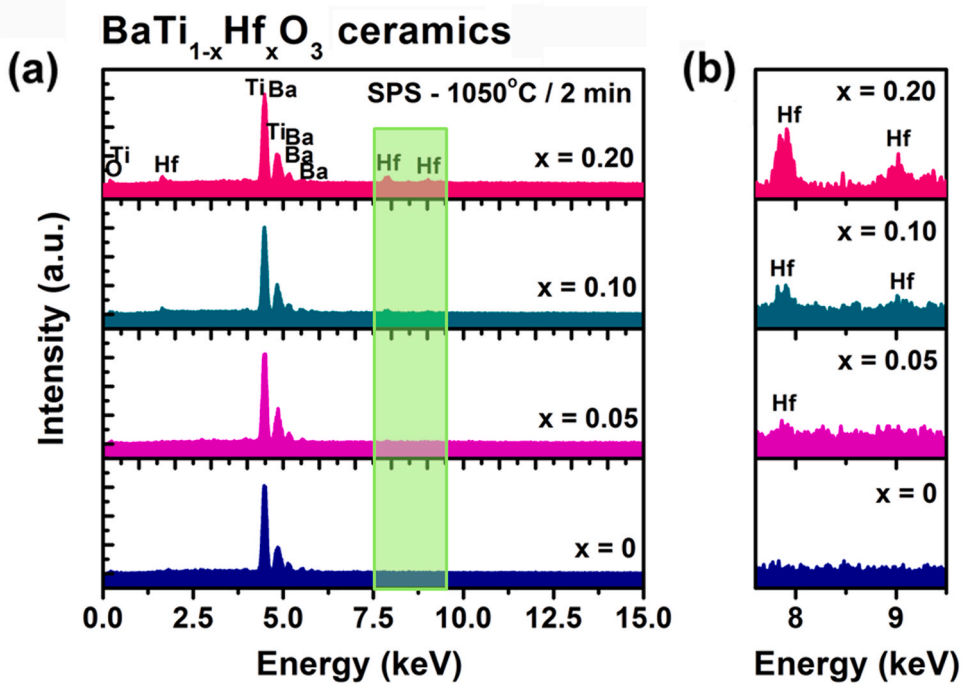

Fig. 7. (a) EDX spectra of the $BaTi_{1-x}Hf_xO_3$ ceramics derived from the Pechini nanopowders and consolidated by SPS at 1050°C / 2 min and (b) detail (the light green rectangle of Fig. 7(a)) of the region corresponding to the energy range $E = 7.5 - 9.5$ keV, showing the variation of intensity of the main Hf peaks with the increase of substitution degree, x.

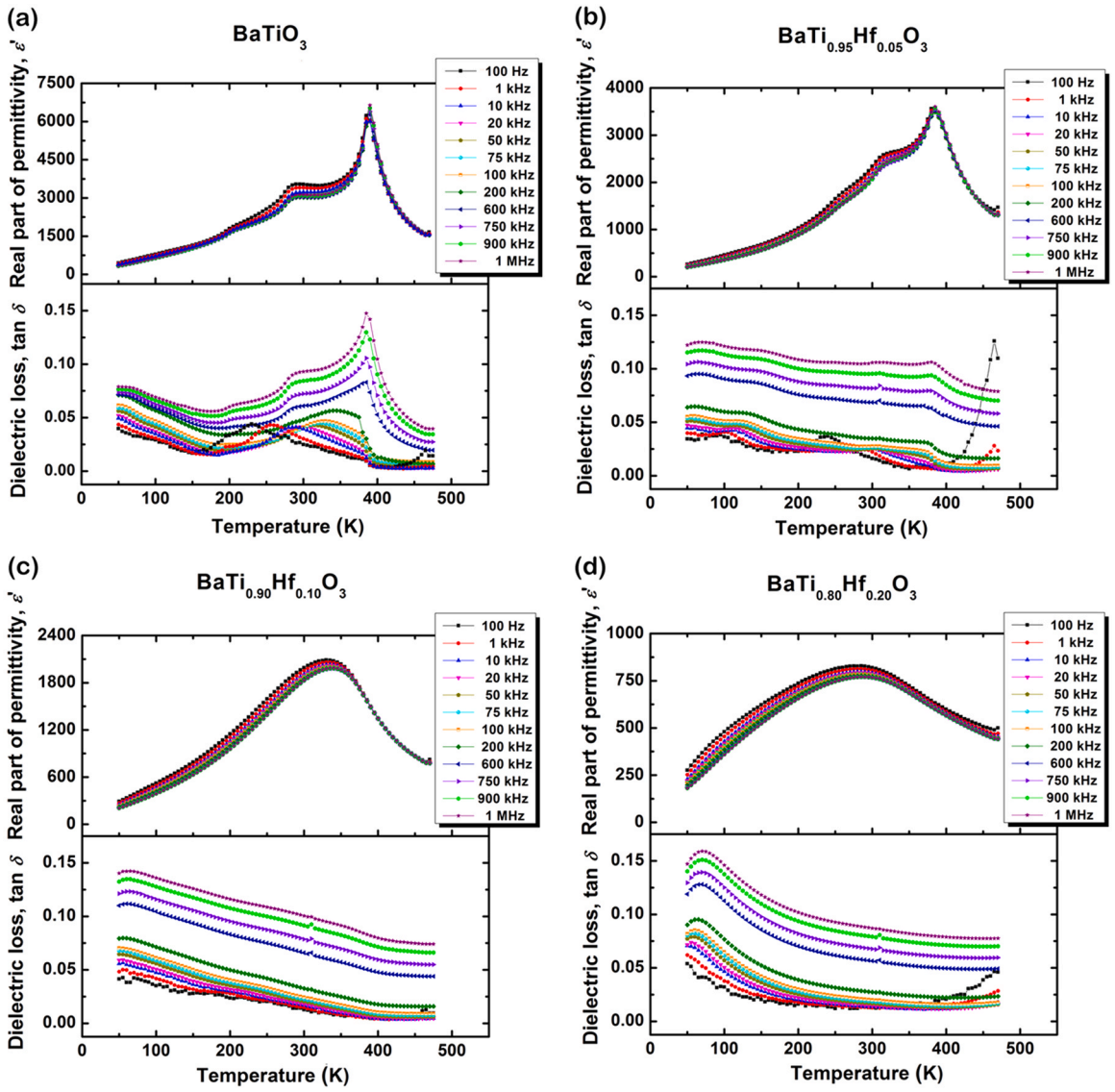

Fig. 8. Temperature dependence of the real part of permittivity (ε′) and the dielectric losses (tan *δ)* at fixed frequency values ranged between (10^2 – 10^6) Hz for the ceramics under investigation: (a) BT; (b) BTH05; (c) BTH10 and (d) BTH20.

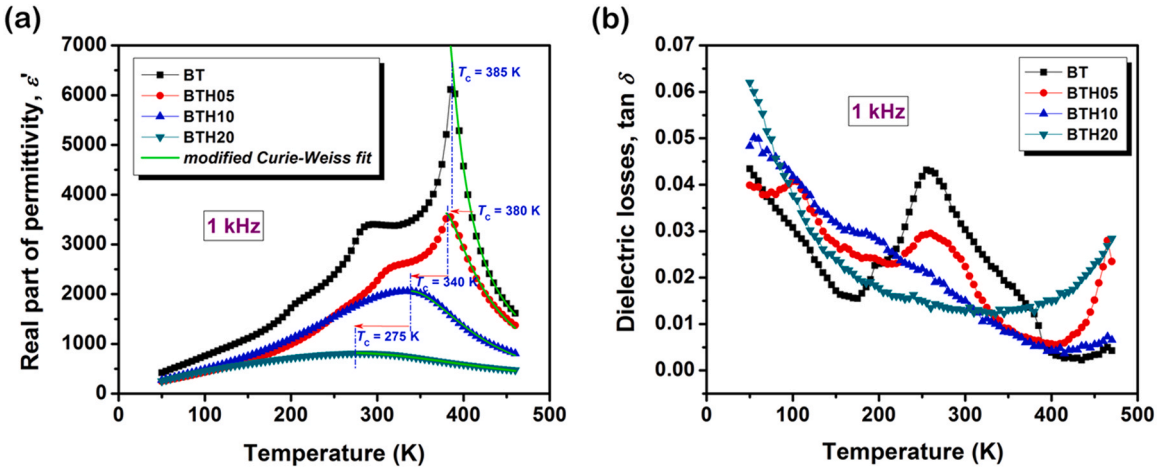

Fig. 9. (a) Temperature dependence of the permittivity, ε′ and analysis according to the modified Curie – Weiss law and (b) temperature dependence of the dielectric losses, tan *δ(T)* at a fixed frequency of 1 kHz for all the BTH ceramics under investigation.

Table 5
Experimental data and fit parameters for BTH ceramics for a frequency of 1 kHz.

Sample	ε'_A	ε'_m	T_A (K)	T_C (K)	γ	δ (K)	T_1 (K)	T_2 (K)	ε'_{RT}	tan δ at RT
BT	6983	6113	389	385	1.13	4.7	290	205	3404	0.030
BTH05	3627	3560	380	380	1.27	8.5	315	260	2174	0.022
BTH10	2060	2059	340	340	1.74	35.5	-	-	1922	0.015
BTH20	817	812	275	275	1.84	96.8	-	-	808	0.013

At high frequencies ($> 10^5$ Hz), tan δ increases for all samples, converging to similar values. This rise at high frequencies is typically associated with conduction-related losses, where mobile charge carriers contribute to the energy dissipation. The lower increase in tan δ for BTH10 and BTH20 indicates that higher Hf concentrations reduce the impact of conduction mechanisms, most likely due to structural modifications that limit charge transport pathways. Unlike in the paraelectric state, in the ferroelectric phase a broad peak appears at intermediate frequencies ($\sim 10^2$ – 10^4 Hz), suggesting the presence of dielectric relaxation mechanisms, possible related to localized dipolar fluctuations. The suppression of this peak in BTH10 and BTH20 indicates that higher Hf doping reduces dipolar relaxation effects, leading to a more stable dielectric response. At high frequencies ($>10^5$ Hz), tan δ increases similarly across all compositions, though the rate of increase is slightly lower for BTH10 and BTH20 compared to BT. This evolution indicates that hafnium incorporation mitigates high-frequency dielectric losses by suppressing conduction-related effects.

The observed decrease in ε' and loss reduction over the entire frequency range, coupled with the dielectric loss associated to the domain-related features in ε'' and tan δ, confirms that increasing Hf content promotes a transition toward a more diffuse phase transition and relaxor-like behaviour. This aligns well with the Curie-Weiss fitting results, where the diffuseness parameter (γ) and broadening parameter (δ) systematically increased with Hf content.

To further quantify the dielectric relaxation behaviour, the complex permittivity data were analysed using the Havriliak–Negami (HN) model, widely used to describe non-Debye relaxations in disordered ferroelectric and relaxor materials. The HN function, which generalizes the Debye response, is expressed as [74]:

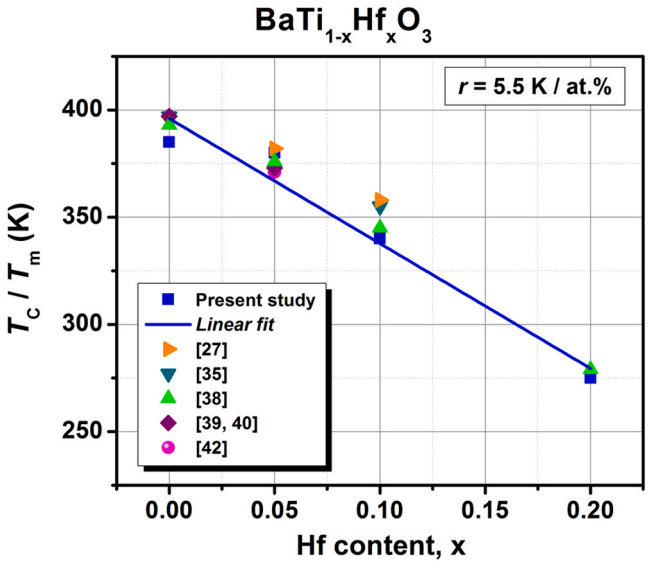

Fig. 10. Dependence of ferroelectric-paraelectric phase transition temperature, T_C / T_m, *vs.* Hf content for BTH ceramics consolidated by spark plasma sintering investigated in this study, as well as for BTH ceramics consolidated by conventional sintering, reported in the literature [23,25–27,35,38–40,43].

$$\varepsilon^*(\omega) = \varepsilon_\infty + \frac{\Delta\varepsilon}{[1 + (i\omega\tau)^{\alpha_{HN}}]^{\beta_{HN}}}, \quad \varepsilon^*(\omega) = \varepsilon'(\omega) - i\varepsilon''(\omega), \tag{2}$$

where $\varepsilon^*(\omega)$ is the complex permittivity, ε_∞ the high-frequency permittivity and $\Delta\varepsilon = \varepsilon_\infty - \varepsilon_0$ is the dielectric strength. The parameters α ($0 < \alpha_{HN} \leq 1$) and β ($0 < \beta_{HN} \leq 1$) account for the symmetric and asymmetric broadening of the relaxation peak, respectively, while τ is the characteristic time.

The model was fitted to the frequency-dependent dielectric data at both 250 K ($T < T_C$) and 425 K ($T > T_C$), and the resulting parameters are presented in Fig. 11(g) and (h) as a variation of the Hf content. As seen at low temperature (250 K, Fig. 11(h)), the α_{HN} parameter remains close to unity for the BT and BTH05 compositions, indicating narrow relaxation behaviour and it reduces when increasing Hf content, thus reflecting a progressive deviation from Debye-like behaviour as disorder increases. The β_{HN} parameter increases with Hf concentration as result of enhanced asymmetry in the relaxation process, which is characteristic of polar nanoregions and relaxor-like systems. The evolution of both α_{HN} and β_{HN} parameters strongly supports the conclusion that Hf doping introduces structural disorder and induces a crossover from classical ferroelectric to relaxor behaviour, dominated by localized dipolar fluctuations. Simultaneously, both the static permittivity ε_0 (extrapolated to $\omega \to 0$) and the high-frequency permittivity ε_∞ show a decay trend with increasing Hf content. This behaviour confirms that Hf substitution weakens the long-range ferroelectric interactions, enhances structural disorder, and promotes a crossover to a relaxor-type behaviour. At high temperature (425 K, Fig. 11(g)), α_{HN} remains nearly constant and close to unity for all the compositions, while β_{HN} shows a slight decrease with increasing Hf content. This change suggests that, above T_C, the system exhibits more Debye-like behaviour, where the relaxation becomes broader and more symmetric despite the structural disorder due to isolated dipolar relaxations, typical for uncorrelated polar fluctuations in the paraelectric phase. Thus, the relaxation dynamics above T_C become more uniform, governed by localized mechanisms, even in compositions with high disorder. The static (ε_0) and high-frequency (ε_∞) permittivity decrease systematically with increasing Hf content, further confirming the suppression of long-range ferroelectric order and the progressive dominance of intrinsic, localized polarization processes in heavily Hf-doped ceramics.

3.2.3.3. Charge transport mechanisms. To further investigate the charge transport mechanisms in Hf-doped BT ceramics, the frequency dependence of the a.c. conductivity ($\sigma_{a.c.}$) and the Nyquist plot (ReZ *vs.* ImZ) were analyzed in Fig. 12 at 470 K, a temperature well above the Curie point, where all the compositions are in the paraelectric phase.

The general trend observed in Fig. 12(a) reveals that $\sigma_{a.c.}(f)$ increases with frequency for all compositions. This behaviour is consistent with a conduction mechanism influenced by both long-range charge transport and localized hopping processes. The impact of hafnium doping is evident in both the absolute values of conductivity and the evolution of the frequency exponents. The frequency-dependent conductivity $\sigma_{a.c.}(f)$ in dielectric materials can be described using Jonscher's universal power law [75], which accounts for both the d.c. and a.c. contributions to conduction. The equation is given as:

$$\sigma_{a.c.}(f) = \sigma_{d.c.} + A\omega^s \tag{3}$$

where $\sigma_{d.c.}(f)$ is the d.c. conductivity, representing the frequency-independent contribution at low frequencies, dominated by long-range charge transport, A is the pre-exponential factor that depends on the material properties and temperature, ν is the frequency of the applied field, $\omega = 2\pi f$ is the angular frequency, and s is the frequency exponent. However, for materials with complex conduction and relaxation behaviour, such as doped BT systems, a single power law term may oversimplify the physical processes at play. This is particularly evident in doped ceramics where contributions from structural defects and multiple mechanisms coexist. To address this, the equation can be expanded to include a second power law term:

$$\sigma_{a.c.}(f) = \sigma_{d.c.} + A_1\omega^{s_1} + A_2\omega^{s_2}, \quad (4)$$

where the parameters A_1, A_2, s_1 and s_2 capture the distinct contributions from different conduction and relaxation processes in the low and high frequency regions of the $\sigma_{a.c.}(f)$. The exponents s_1 for low-frequency transport ($0 \leq s_1 \leq 1$) and s_2 for high-frequency relaxations ($1 \leq s_2 \leq 2$) provide insight into the nature of the conduction and relaxation mechanisms across the entire frequency range and separate contributions from different mechanisms characterizing the BTH ceramics.

The frequency exponent s_1 provides information about the strength of dispersive charge transport at low frequencies ($< 10^4$ Hz). Undoped BT ($s_1 = 0.48$) exhibits the lowest exponent, indicating a relatively easier charge transport, which aligns with the previously observed higher dielectric losses and more significant conduction-related effects. BTH05 ($s_1 = 0.54$) shows a slight increase in s_1, suggesting that the introduction of small amounts of Hf slightly hinders the long-range movement of charge carriers, possibly due to local distortions in the perovskite lattice. BTH10 ($s_1 = 0.71$) and BTH20 ($s_1 = 0.73$) display a significant increase in s_1, implying a more restricted charge transport. The higher values suggest that increasing Hf concentration leads to stronger localized effects, consistent with the previously observed reduction in dielectric losses and the transition toward relaxor-like behaviour. Higher Hf doping reduces the long-range mobility of charge carriers, reinforcing the idea that structural modifications induced by Hf incorporation limit inter-site charge transport. The increase in s_1 with Hf content is consistent with the stabilization of the dielectric response and the suppression of conduction-related losses.

The exponent s_2 provides insight into the dispersive nature of charge transport mechanisms at high frequencies ($>10^5$ Hz). For undoped BT ($s_2 = 1.97$) and BTH05 ($s_2 = 2.00$) the values close to 2 indicate that the

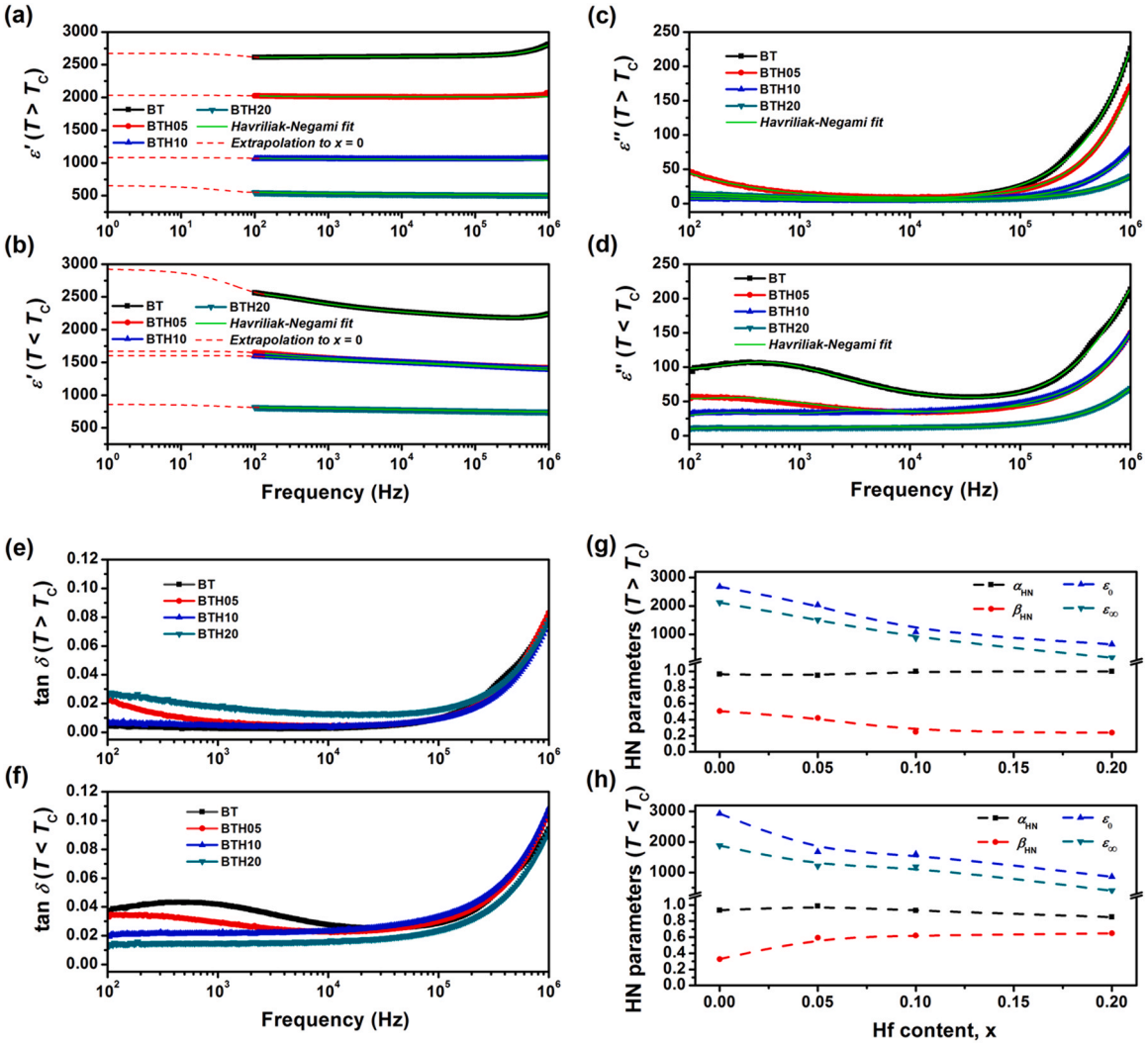

Fig. 11. Frequency dependence of the real part of permittivity $\varepsilon'(f)$: (a) above the T_C and (b) below the T_C; frequency dependence of the imaginary permittivity $\varepsilon''(f)$: (c) above the T_C and (d) below the T_C and frequency dependence of the dielectric losses tan $\delta(f)$: (e) above the T_C and (f) below the T_C for the BTH ceramics; variation of Havriliak–Negami fitting parameters as a function of Hf content: (g) in the paraelectric region above the T_C, (h) in the ferroelectric region below the T_C. The green solid lines in panels (a)–(d) represent the Havriliak–Negami model fit, while the red dashed lines in panels (a) and (b) indicate the extrapolated values of ε' toward zero frequency (ε_0).

high-frequency conduction is better associated with a nearest-neighbour hopping mechanism or highly localized charge motion rather than with extended hopping between distant localized states, according to Funke's model [72]. This interpretation is consistent with the presence of a significant structural disorder, where charge carriers move between localized states. BTH10 ($s_2 = 1.5$) and BTH20 ($s_2 = 1.5$) show a significant decrease in s_2, suggesting that the conduction process becomes increasingly dominated by localized polarization fluctuations rather than hopping transport. This finding supports the previously observed suppression of dielectric relaxation losses (tan $\delta(f)$) and indicates that charge carriers in the heavily Hf-doped ceramics undergo stronger trapping effects, limiting their ability to participate in long-range transport.

Fig. 12(b) enables the separation of contributions from low- and high-frequency processes through a detailed complex impedance analysis at 470 K, based on fitting using the equivalent circuit described in Fig. 12(c). This approach decouples the contributions of different microstructural components, such as grain cores, grain boundaries, and interfaces, whose contributions manifest over distinct frequency ranges.

The equivalent circuit employed to fit the experimental data includes a serial resistance R_S connected with a simple R_g/C_g element to model the bulk grains, which dominates the high-frequency region and reflects intrinsic transport and relaxation properties within the crystalline domains. The grain boundaries are represented by an R_{gb}/C_{gb} element, dominating the intermediate frequency range, where higher resistive and capacitive contributions arise due to defect accumulation and structural discontinuities or reticular disruption at intergranular regions. The strong agreement between the experimental data and the fitted curves validates the proposed equivalent circuit model for accurate describing the impedance behaviour of the undoped BT specimen, as well as for the Hf-doped (BTH) ceramics. The resistances and relaxation times derived from the equivalent circuit, associated with the grains and grain boundaries, are shown as a function of the Hf doping level in Fig. 12(d), (e).

The fitting parameters obtained from the Jonscher power-law, as well as the characteristics of the proposed equivalent circuit are summarized in Table 6.

Fig. 12(d) and Fig. 12(e) illustrate the grain core/grain boundary

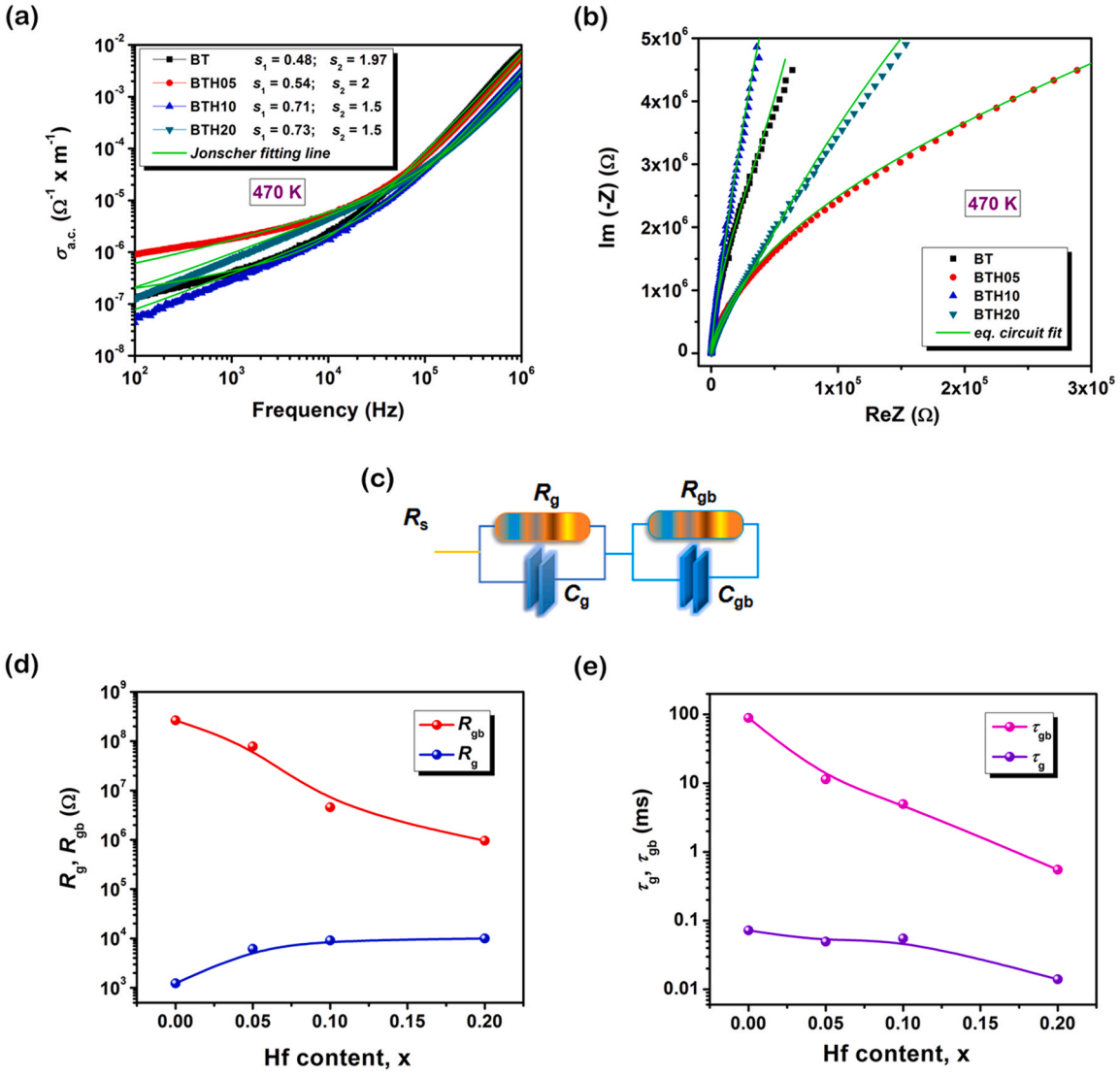

Fig. 12. (a) Frequency dependence of a.c. conductivity $\sigma_{a.c.}(f)$, and (b) Nyquist plot of the impedances measured at a fixed temperature of 470 K for undoped and Hf-doped BT ceramics, (c) the equivalent circuit used to fit the experimental data in (b); variation of (d) grain and grain boundaries resistance determined based on the equivalent circuit fitting and of (e) grain and grain boundaries time constants as a function of the hafnium content. The solid green lines represent the fittings performed as follows: in (a) using the Jonscher's power-law with the extracted frequency exponents (s_1 and s_2) indicated in the legend and in (b) using the proposed equivalent circuit.

Table 6
Fitting parameters extracted from the equivalent circuit modeling for the BTH ceramics.

Sample	s_1	C_g (F)	C_{gb} (F)	R_s (Ω)	R_g (Ω	R_{gb} (Ω)	τ_g (ms)	τ_{gb} (ms)
BT	0.48	3.4×10^{-10}	5.6×10^{-8}	44	1.2×10^{3}	2.6×10^{8}	7.2×10^{-5}	8.9×10^{-2}
BTH05	0.54	1.5×10^{-10}	8×10^{-9}	95	6.1×10^{3}	7.8×10^{7}	4.9×10^{-5}	1.1×10^{-2}
BTH10	0.71	1.1×10^{-9}	6×10^{-9}	204	9.1×10^{3}	4.6×10^{6}	5.5×10^{-5}	4.9×10^{-3}
BTH20	0.73	5.7×10^{-10}	1.4×10^{-9}	288	9.9×10^{3}	9.5×10^{5}	1.4×10^{-5}	5.5×10^{-4}

resistances and relaxation times as a function of Hf content in BTH ceramics. The grain resistance R_g associated with the bulk transport properties exhibits an initial more pronounced enhancement with increasing solute content, followed by its stabilization at higher Hf proportions. This suggests that the incorporation of Hf into the BT lattice modifies the electronic structure and reduces intrinsic charge carrier mobility, leading to an increased bulk resistivity. The stabilization of R_g at higher substitution degrees indicates that the system reaches a new equilibrium state, where additional Hf does not significantly alter bulk conductivity. The grain boundary resistance R_{gb} which indicate the blocking effect of grain boundaries on charge transport decreases systematically with increasing Hf content. This reduction suggests that Hf doping alters the grain boundary structure, possibly by reducing the concentration of defect states or charge trapping centres that typically

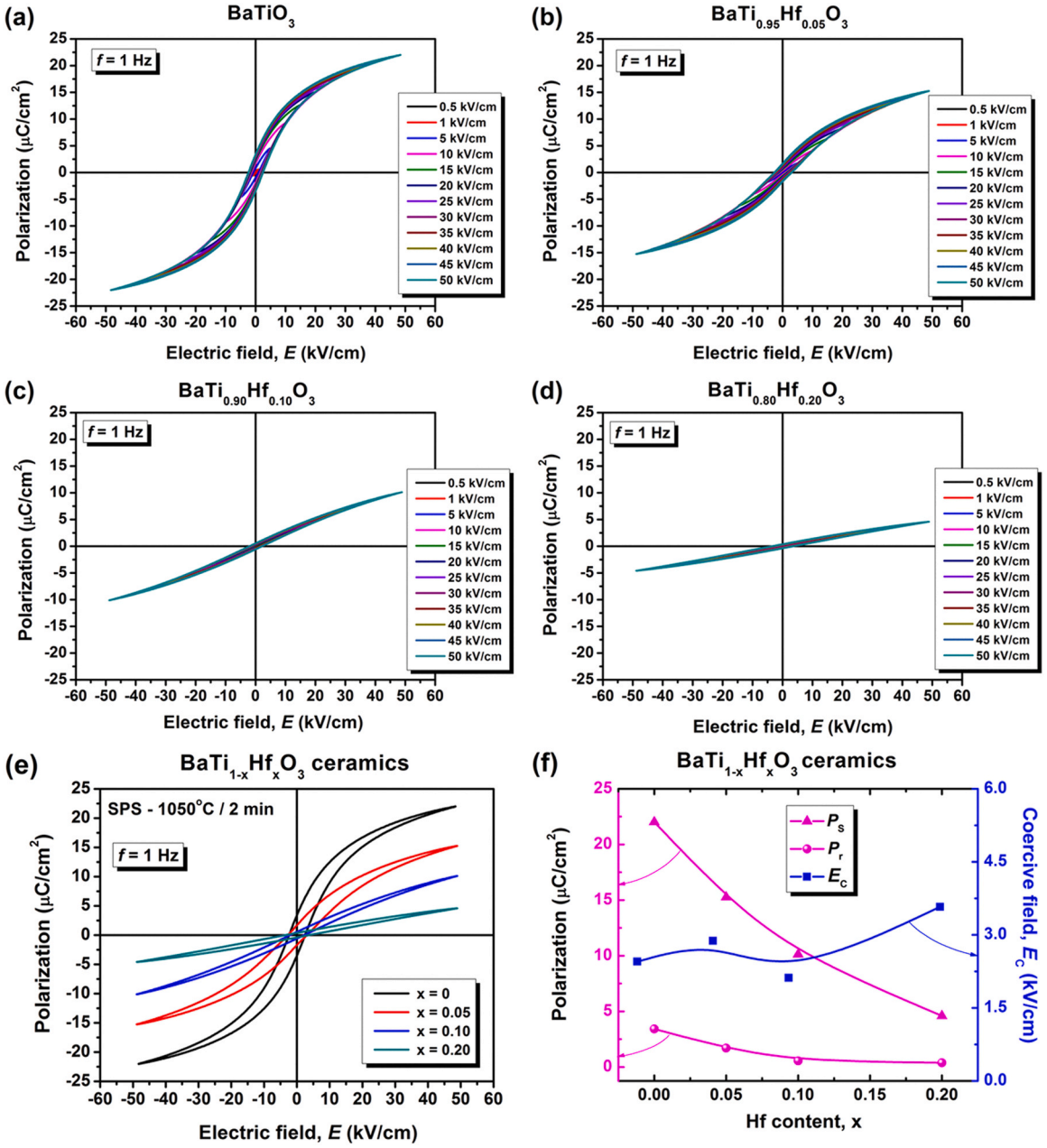

Fig. 13. (a)-(d) *P*(*E*) ferroelectric hysteresis loops determined at room temperature (frequency of 1 Hz), under variable electric field amplitudes for the $BaTi_{1-x}Hf_xO_3$ ceramics with compositions: (a) x = 0; (b) x = 0.05; (c) x = 0.10, (d) x = 0.20; (e) comparative hysteresis loops recorded at the maximum applied electric field and (f) P_S, P_r, and E_C evolution *vs*. Hf content corresponding to BTH ceramics.

contribute to high resistive barriers.

The significant decrease in R_{gb} implies that grain boundaries become more conductive as Hf concentration increases, facilitating a certain degree of charge transport across grain interfaces. The relaxation time constants associated with the grain (τ_g) and grain boundary (τ_{gb}) contributions allow a deeper insight into the polarization dynamics and charge transport processes in Hf-doped BT ceramics. The grain boundary relaxation time (τ_{gb}) exhibits a systematic decrease with increasing Hf content, spanning nearly two orders of magnitude. This trend indicates that the polarization response at grain boundaries becomes progressively faster with Hf doping, suggesting that the potential barriers at the interfaces are lowered. The reduction in τ_{gb} aligns with the previously observed decrease in R_{gb}, confirming that charge transport across grain boundaries becomes less resistive as a consequence of Hf incorporation.

The grain relaxation time (τ_g) also decreases with increasing Hf content, but the reduction is much less pronounced than for τ_{gb}. This suggests that bulk polarization dynamics are affected by Hf doping, but to a lesser extent than at the grain boundaries. The decrease in τ_g correlates with the increase in R_g, indicating that the bulk response remains resistive but with faster relaxation dynamics, potentially due to enhanced local polarization fluctuations characteristic of relaxor-like behaviour.

The correlation between the a.c. conductivity exponent (s_1), series resistance (R_S), and relaxation parameters further supports these trends. The increase in s_1 with Hf content indicates a shift from long-range conduction toward more dispersive transport mechanisms, consistent with the increase in R_g and the stabilization of bulk resistivity. The systematic decrease in R_{gb} and τ_{gb} suggests that grain boundaries become progressively less resistive, facilitating faster charge transport across interfaces. Meanwhile, the increase in R_S reflects a reduction in the free charge carrier concentration, reinforcing the localized nature of polarization dynamics. The alignment of these parameters confirms that Hf doping suppresses long-range ferroelectric interactions, promotes localized conduction mechanisms and enhances ferroelectric-relaxor crossover in BTH ceramics.

The evolution of the relaxation times τ_g and τ_{gb} can be directly correlated with the increased density of grain boundary states, particularly in the BTH10 and BTH20 ceramics, where the grains are downscaled toward the nanometre range. Thus, the sharp decrease in τ_{gb} with increasing Hf content suggests that charge transport across grain boundaries becomes progressively faster, most likely due to nanostructuring. This trend aligns with the previously observed reduction in R_{gb}, confirming that the grain boundary regions become more conductive as their number increases, thereby facilitating charge transport. The pronounced reduction of τ_{gb} in BTH10 and BTH20 supports the idea that a higher density of grain boundaries enhances interfacial polarization dynamics, allowing faster relaxation processes. This increased interfacial contribution, coupled with the reduced long-range ferroelectric interactions in the bulk, reinforces the transition toward a more localized, ferroelectric-relaxor crossover in the heavily-doped BTH specimens. In contrast, τ_g exhibits a more gradual decrease, which, together with the increase in R_g, indicates that, while bulk polarization dynamics are affected by Hf doping, the most significant modifications occur at the grain boundaries.

3.2.4. High-field properties

3.2.4.1. Ferroelectric hysteretic P(E) response. Ferroelectric $P(E)$ loops of the coarse $BaTi_{1-x}Hf_xO_3$ ceramics with a few similar compositions have been reported in refs. [35,36,38–41]. However, well saturated loops recorded for a high applied fields with amplitude around 30 – 45 kV/cm, to allow a comparison of their characteristics, are presented only in refs. [38–40]. For the present compositions, Fig. 13(a)-(d) shows the evolution of the $P(E)$ hysteresis loops and the switching characteristics as a function of the Hf content. All the investigated ceramics sustained the application of a high field of ~50 kV/cm amplitude, enough to provide saturation and to exhibit a stable polarization-field switching response, with symmetrically shaped and well-closed hysteresis loops. With respect to the $P(E)$ loops reported in literature for coarse BTH ceramics, all the BTH ceramics under investigation show lower values for the hysteresis loop area, rectangularity factor P_r/P_S (below 0.16) and similar values as in literature for the coercive field (E_C) (Fig. 13(e), (f)) [38–40]. The remanent polarization P_r takes values below 5 μC/cm^2 for all the fine-grained investigated BTH compositions (Fig. 13(f)), while for coarse ceramics with similar or close compositions, larger values have been reported in literature: 12 – 15 μC/cm^2 (for Hf: 5 % and 11 %) [39], 14 μC/cm^2 (5 % Hf) and 8 μC/cm^2 (12 % Hf) [40], 7 – 10 μC/cm^2 (2 % Hf) [41]. This result represents a typical grain size effect, as ones recorded in BT-based ceramics when reducing their grain size at nanoscale [44,48,50,53,66].

The $P(E)$ hysteresis loops become progressively less saturated and more tilted when increasing the Hf addition, so that the rectangularity factor decreases down to 0.08 value for BTH20. The polarization response is scaled down with Hf addition, with a saturation polarization from $P_S \sim 22$ μC/cm^2 in pure BT ceramic to $P_S \sim 10$ μC/cm^2 for the composition x = 0.10. The composition BTH20 shows a very tiny hysteretic behaviour, but still presents a very small non-linearity. Usually, it has been reported that the relaxor behaviour induced by such substitutions leads to a pronounced polarization reduction and tilting of the $P(E)$ hysteresis loops [11,14,33,36]. This tendency demonstrates the gradual transformation of the dipolar entities from long-range-order ferroelectric character to the relaxor state characterized by nanoscale polarization, which is characterized by practically zero coercivity. The small polarization values and the slim and tilted hysteresis loops are also a consequence of the approaching at room temperature the range for the ferroelectric-to-paraelectric transformation when increasing the Hf addition, and is also a characteristic of the nanostructured BT-based ceramics [44,48–50,53,66]. Therefore, the strong polarization reduction, the gradual increase of the loop tilting towards a non-hysteretic polarization-field response observed for the BTH ceramics can be comprehended by the three combined factors induced by the increasing Hf substitution: the ferroelectric-relaxor crossover, the grain size reduction down to nanoscale and the approaching of the paraelectric cubic state around room temperature.

The energy storage performance is evaluated by three main parameters: the stored energy density, the recoverable energy density, and the energy storage efficiency. These properties are determined using the following Eqs. (5) - (8) [76]:

$$W_{rec} = \int_{Pr}^{Pmax} EdP \tag{5}$$

$$W_{stor} = \int_{0}^{Pmax} EdP \tag{6}$$

$$W_{loss} = W_{stor} - W_{rec} \tag{7}$$

$$\eta = \frac{W_{rec}}{W_{rec} + W_{loss}} \times 100 \tag{8}$$

The density of energy storage, W_{stor}, energy loss, W_{loss} and recoverable energy, W_{rec} of the $BaTi_{1-x}Hf_xO_3$ ceramics are presented in Fig. 14. The Hf addition induces a gradual reduction of the stored energy density, W_{stor}, from 361 mJ/cm^3 for BT, 313 mJ/cm^3 for x = 0.05, 235 mJ/cm^3 for x = 0.10 and 118 mJ/cm^3 for x = 0.20, as well as of the recoverable energy, W_{rec}, from 269 mJ/cm^3 for BT, 236 mJ/cm^3 for x = 0.05, 205 mJ/cm^3 for x = 0.10 down to 94 mJ/cm^3 for x = 0.20. It is worth to be mentioned that the decrease in W_{loss} was from 93 mJ/cm^3 in the case of pure BT to 24 mJ/cm^3 for x = 0.20. The yield (storage efficiency), η, is 74 % for BT and increases with Hf content up to the highest value of 87 % for the composition x = 0.10. For the nanocrystalline BTH10 and BTH20 ceramics analyzed here, the energy

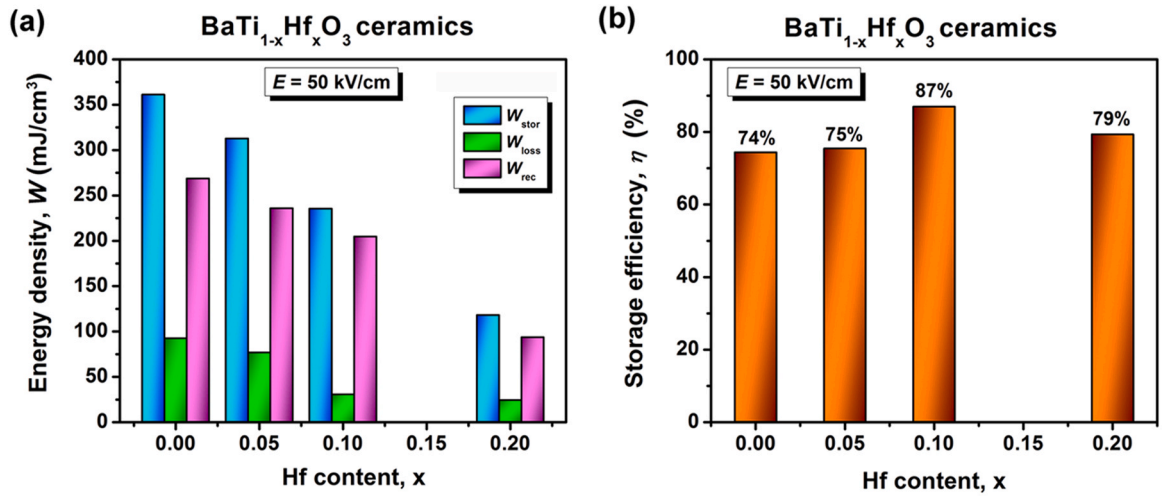

Fig. 14. Dependence on Hf content for: (a) energy storage density – W_{stor}, energy loss density – W_{loss} and recoverable energy density – W_{rec} and (b) storage efficiency – η, estimated at an electric field $E = 50$ kV/cm.

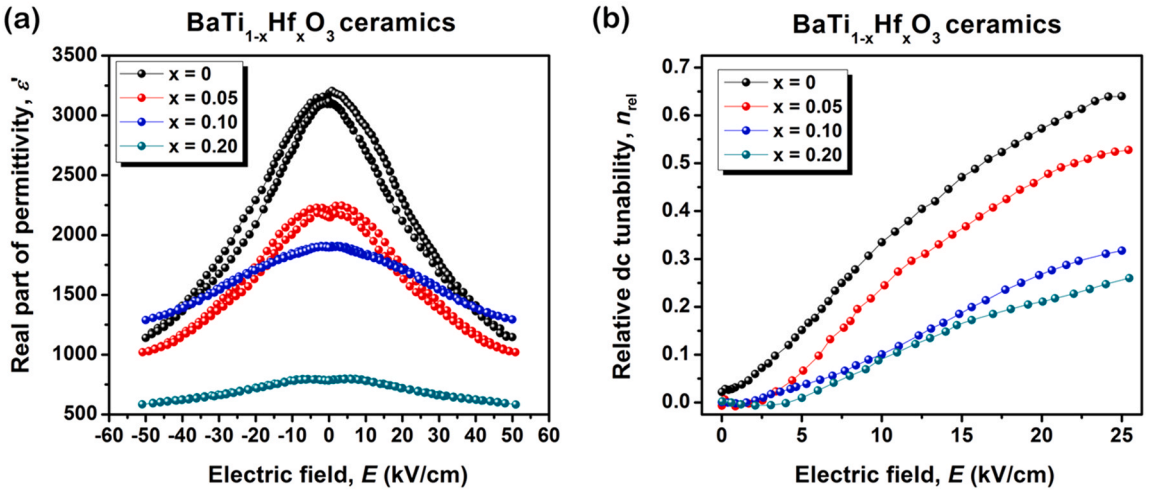

Fig. 15. (a) Real part of permittivity, ε' *vs.* dc-electric field under an increased/decreased field cycle and (b) relative dc-tunability *vs.* applied dc-field calculated for all the BTH ceramics under investigation.

storage efficiency reaches higher values compared with those corresponding to the fine-grained $Ba_{0.6}Sr_{0.4}TiO_3$ ceramics with almost similar grain size, previously investigated ($\eta \sim 70$ %) [52].

3.2.4.2. Non-linear dielectric properties (tunability). Tunability, *i.e.* the dc field-dependence of the dielectric constant was not reported till now for any BTH ceramics. The non-linear dielectric behaviour was investigated by measuring the variation of the real part of permittivity *vs.* d.c. field under a complete increase/decrease dc field cycle (dc-tunability), up to the field amplitude of ± 50 kV/cm, starting from a depolarized state (Fig. 15(a), (b)). The dielectric losses remained below 7 % for all the investigated compositions, at any applied field, thus indicating the excellent dielectric character of all the BTH samples under high d.c. fields. All the compositions show a stable, well-reproducible non-linear dielectric character, *i.e.* the permittivity is not constant under the application of d.c. field cycles (Fig. 15(a)). The relative permittivity indicates a tendency to saturation (still not reached), for d.c. fields above 40 kV/cm. As expected, the hysteretic nature of the $\varepsilon'(E)$ curve tends to reduce at high Hf content, as result of the proximity of the ferroelectric-to-paraelectric transition and to the ferroelectric-relaxor crossover, indicated by the low field dielectric properties and Raman analyses. Practically, the hysteresis of $\varepsilon'(E)$ is not anymore observed at all for the compositions x = 0.10 and 0.20, although the nonlinear dielectric character is still maintained. For any field value, a permittivity reduction with increasing the Hf addition is observed. However, this reduction ratio is not the same at each d.c. field value. For example, if at zero field the ratio between the permittivity of BT and one of the BTH20 sample is of ~4.33, this ratio downgrades to only ~2, under the dc field of 50 kV/cm. Furthermore, at this maximum field value, the permittivity of BTH10 is even higher than one of the BT ceramics under the same field. By considering that towards saturation, the extrinsic domain walls contribution to the permittivity is strongly reduced by the tendency of forming a single-domain state, it results that high d.c. fields suppress such contributions mostly for the BT and BTH05 compositions and far less for BTH10 and BTH20 ultra-fine ceramics. Moreover, the fact that for both the BTH10 and BTH20 ceramics, the saturation has not yet been observed up to 50 kV and their permittivity decay has a lower rate than for the other two samples, denotes that in the ultrafine ceramics the domain walls are pinned (most probable by the large number of grain boundaries) and cannot be easily moved to form a single-domain state, like in the case of microsized ceramics. A similar effect denoted as „frozen polarization" determined by nanostructuring was reported for ultrafine BT ceramics [48–50]. Therefore, the two BTH10 and BTH20 compositions represent an interesting combination of relaxor-like

systems with fluctuating nanopolar domains (and ultra-small coercivity) and frozen-like polarization regions, which need huge field values to be moved, being characterized by an enormous coercivity. Both these effects cause a reduction of the polarization-field and permittivity-field response and of their corresponding hysteresis loops at high Hf additions, together with the reduction of ferroelectric-to-paraelectric transition temperature.

The relative dc-tunability, n_r is calculated using the Eq. (9) and its variation as a function of the electric field is presented in (Fig. 15(b)):

$$n_r = \frac{\varepsilon(0) \quad -\varepsilon(E)}{\varepsilon(0)} \tag{9}$$

The relative dc-tunability of dense BT ceramic is $n_r = 64$ % for the maximum applied field of $E_{dc} = 50$ kV/cm (Fig. 15(b)). With increasing Hf amount, the relative dc-tunability presents a continuous decrease, *i.e.* $n_r = 53$ % for x = 0.05, $n_r = 32$ % for x = 0.10, and $n_r = 26$ % for x = 0.20. Nanostructuring in BTH10 and BTH20 specimens strongly affects the dc-tunability, whose values are significantly lower than in other homovalently *B*-site doped microstructured BT ceramics with similar compositions, as BTSn ceramics ($n_r \sim 74$ % for BTSn10 and $n_r \sim 55$ % for BTSn20) [10]. On the other hand, the highest value of the relative dc-tunability obtained in this study for BTH05 is larger than the values reported for some (Ba,Sr)TiO_3 ceramics ($n_r \sim 30$ %) [77] and related BST/MgO composites ($n_r \sim 40$ %) [78]. Moreover, the tunability values obtained for nanocrystalline BTH10 and BTH20 specimens are significantly higher than that one reported for the nanostructured $Ba_{0.6}Sr_{0.4}TiO_3$ ceramic sample ($n_r \sim 8$ %) with almost similar grain size resulted after consolidation by SPS [52]. It is worthwhile to note this result, which is highly important for possible tunable applications, since a permittivity below 1000 combined with the lack of hysteresis and reasonable values of tunability is reached by Hf substitution and nanostructuring.

3.2.5. *Short-range ordering and evolution of phase transitions vs. temperature by Raman spectroscopy investigations*

Raman spectroscopy is a powerful tool, very sensitive in detecting local distortions in perovskite systems where disorder or disruption in crystalline lattice occurs due to doping or to nanoscale structuring.

At room temperature, undoped $BaTiO_3$ is ferroelectric with a T structure. Therefore, the Raman spectrum of bulk $BaTiO_3$ ceramics show the specific features of the T phase, *i.e.* sharp peaks corresponding to the phonon modes located at 90 cm^{-1} [*E*(TO)], 180 cm^{-1} [$A_1(TO_1)$] and 305 cm^{-1} [B_1, *E*(TO+LO)], as well as asymmetric broad bands at 260 cm^{-1} [$A_1(TO_2)$], 520 cm^{-1} [A_1(TO)+*E*(TO)] and 720 cm^{-1} [A_1(LO)+*E*(LO)]. It is worthy to mention that the sharp interference dip at 180 cm^{-1}, originates in the coupling between A_1 modes. [79,80]. Although according to the symmetry rules the cubic $BaTiO_3$ should be Raman inactive, the last three mentioned bands are still present also in the paraelectric state, becoming even broader and almost symmetrical due to the disorder generated by the displacement of Ti in the octahedra of the perovskite lattice [81,82]. There are some additional Raman modes corresponding to the phonons coupled with electrons which appear or disappear during the phase transitions, when the unit cell symmetry changes [83]. Fig. 16(a) displays the overall room-temperature Raman spectra of the BTH ceramics under investigation. In the spectrum corresponding to the BT sample, all the mentioned modes, specific to the ferroelectric tetragonal perovskite phase, were detected at the following wave numbers: 100, 176, 303, 250, 513 and 714 cm^{-1} (Fig. 16(b), (c)).

Hf incorporation onto Ti sites in $BaTiO_3$ lattice induces more pronounced structural and phononic disorder by modifying the local strain field due to the difference in the ionic radii of Ti^{4+} and Hf^{4+}, as well as electronic disorder, by creating Urbach tail states due to the on-site potential fluctuations [84,85]. These disturbances are highlighted in the room-temperature Raman spectra specific to BTH ceramics (Fig. 16 (a)). A supplementary peak, corresponding to the $A_{1\,g}$ phonon mode was detected at ~800 cm^{-1}. The increase of Hf content determines concurrently the systematic increase of the intensity but also a slight flattening of this band, along with its shift lo lower wave number values, *i.e.* from 803 cm^{-1} for BTH05 to 795 cm^{-1} for BTH20, as indicates the detail of the region of medium/high frequency values denoted as "region II" of Fig. 16(c). Sati *et al.* have clearly proven that this mode is not related to a phase transition, but it is caused by the structural disorder [84], as a result of solute incorporation on Ti sites. Hf^{4+} cations are randomly distributed in BO_6 octahedra, generating internal strains in HfO_6 octahedra, affecting both O−Ti−O bonds and Ti−Hf−Ti chains and breaking short-range translational symmetry [40,42,43,86]. It is worth to mention that this mode became the signature of the *B*-site doping in perovskites and its appearance was also reported for other solutes on Ti sites in $BaTiO_3$ [33,87–90].

More significant changes indicating structural evolution induced by the solute proportion are pointed out in the low wave number region

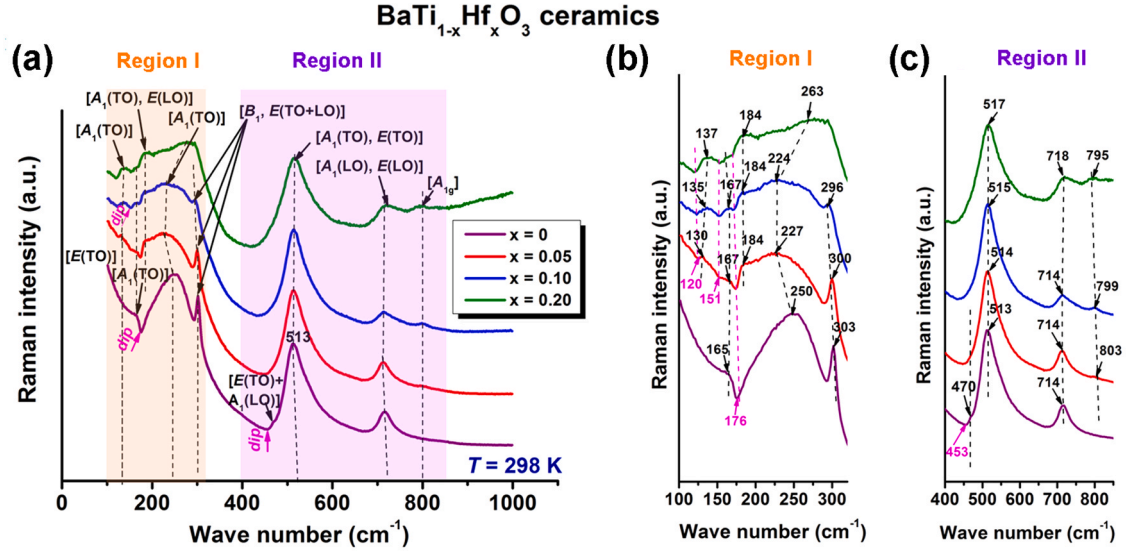

Fig. 16. (a) Raman spectra at room temperature for $BaTi_{1-x}Hf_xO_3$ ceramics consolidated by spark plasma sintering at 1050 °C / 2 min; (b) detail of region I, corresponding to the wave numbers of 100 − 330 cm^{-1} (light orange rectangle of (a)) and (c) detail of region II, corresponding to the wave numbers of 400 − 850 cm^{-1} (light violet rectangle of (a)).

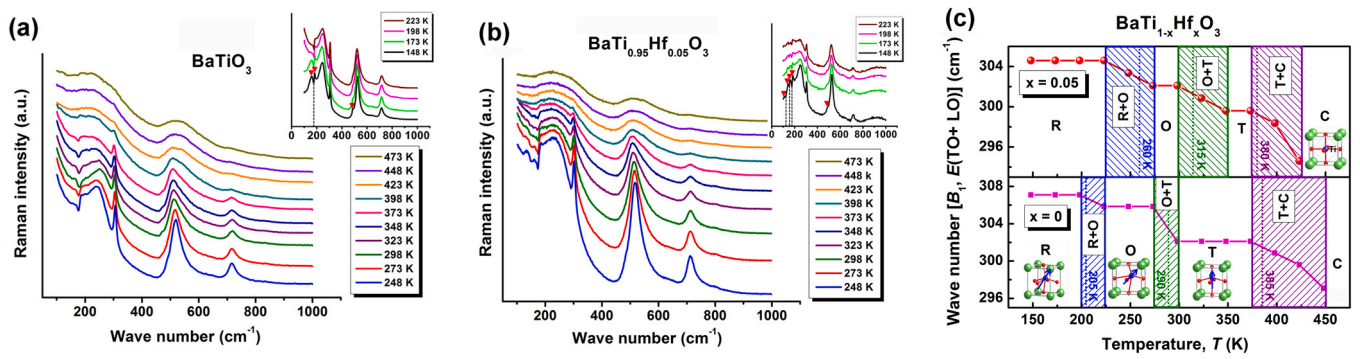

Fig. 17. Overall temperature dependence of Raman scattering in: (a) BT; (b) BTH05 – the insets in the top-right corners of Fig. 17 (a), (b) display the Raman spectra in the temperature range of (148 – 223) K, revealing the features corresponding to the rhombohedral modification (red symbols for R peaks and dashed lines for interferences dip) and (c) temperature dependence of frequency of [B_1, E(TO+LO)] mode in BT and BTH05 ceramics.

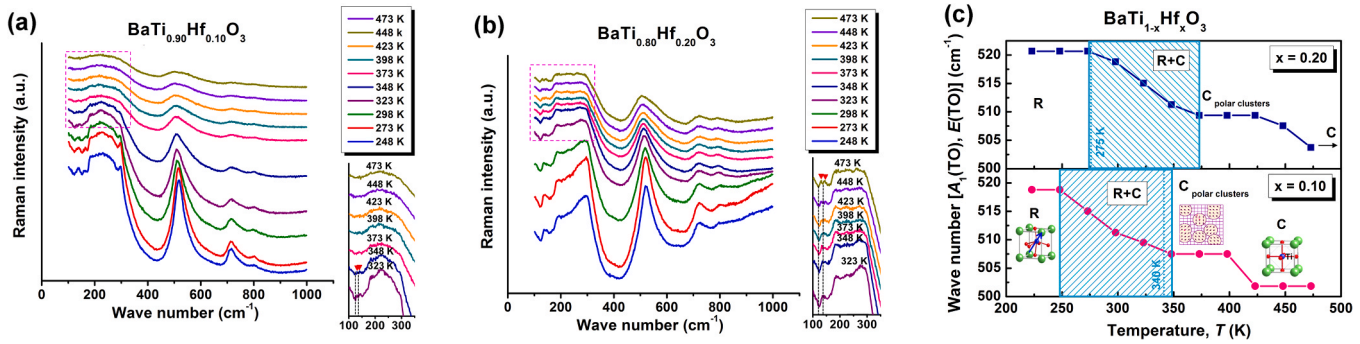

Fig. 18. Overall temperature dependence of Raman scattering in: (a) BTH10; (b) BTH20 – the insets in the bottom-right corners of (a), (b) display details corresponding to the frequency range of 100 – 330 cm^{-1} of the Raman spectra in the temperature range of (323 – 473) K, showing the presence of a residual but stable R order up to 473 K (red symbols for peaks and dashed lines for interferences dip) and (c) temperature dependence of frequency of [A_1(TO), E(TO)] mode in BTH10 and BTH20 ceramics.

denoted as "region I" of the Raman spectra presented in the detail of Fig. 16(b). Thus, the damping of the so-called "silent" mode [B_1, E(TO+LO)] and its downshift from 303 cm^{-1} in BT to 296 cm^{-1} in BTH10, together with the downshift from 250 to 224 cm^{-1} and the gradual flattening until disappearance of the [A_1(TO)] mode, proves a gradual phase transition towards a dissimilar symmetry. For the BTH05 sample the appearance of a new feature at 184 cm^{-1}, assigned to the [A_1(TO)+E(LO)] phonon mode, which is visible as a hump in the left-side of the broad [A_1(TO)] band and the drop in the intensity of the interference dip at 176 cm^{-1} suggests the presence of the orthorhombic distortion [91,92]. This evolution seems to be consistent with the finding resulting from the analysis of the (002)/(200) peak profile in the related XRD pattern of this specimen. For BTH10, the "silent" mode still persists, but the presence of the triple mode, *i.e.* the peaks located at 135, 167, 184 cm^{-1} clearly indicates the rhombohedral structure [33,92–94]. The interference dip at 120 cm^{-1}, as well as that located at 153 cm^{-1} are related to the coupling between A_1(TO) modes, showing that dissimilar [BO_6] octahedra are present in the lattice. These effects are even more clearly marked in BTH20, suggesting that a higher Hf content could determine a certain *B*-site cation ordering into small clusters [95]. The presence of such clusters or polar nanoregions (PNR) originates in a certain structural disorder, which is most likely caused by the difference in the ionic radii, atomic weights and the electronegativities of the host Ti^{4+} cations and of the solute Hf^{4+} species. This can also explain the slim and tilted $P(E)$ hysteresis loop found for BTH20, which exhibits a very small, but still detectable, non-linearity, with a non-zero polarization (P_S = 4.6 μC/cm^2 and P_r = 0.39 μC/cm^2), as already shown above (see Fig. 13(f)). For the BTH10 and BTH20 ceramics the stable R order could also be associated to the nano-sized grains, taking into account that nanostructure in $BaTiO_3$-based solid solutions favours the residual polar order and the overlapping of dissimilarly distorted phases [51–53]. Nevertheless, the strong flattening of the overall Raman spectra for the heavily-doped samples suggests the evolution towards a C structure, especially in BTH20, where the presence of a significant proportion of C phase is proven by the complete disappearance of the silent mode. Overall, one can conclude that the Raman spectroscopy results sustain the XRD data.

To follow the evolution of the structure and to monitor phase transitions in BTH ceramics, the temperature dependence of Raman scattering was recorded in the temperature range of (148 – 473) K, as depicted in Fig. 17(a), (b) and Fig. 18(a), (b).

For the undoped BT specimen, low-temperature features, as the well-marked peaks located at 157 and 183 cm^{-1} and the interference dip between them at 176 cm^{-1}, along with the small shoulder at 486 cm^{-1}, located in the left side of [A_1(TO), E(TO)] mode, prove the presence of the R polymorph in the temperature range of (148 – 173) K (see inset of Fig. 17(a)). The coupling of the modes located at 157 and 183 cm^{-1} is maintained up to 200 K, when the [$A_1(TO_1)$] mode located at ~160 cm^{-1} becomes strongly flattened, while the [A_1(TO), E(LO)] mode is shifted from 183 to 190 cm^{-1}. This feature, together with both the damping of the mode located at 486 cm^{-1}, and the damping and downshift of the [$A_1(TO_2)$] mode located at 226 cm^{-1} indicate that the R structure begins to change into an O modification [96], which seems stable up to 273 K. Further, the gradual disappearance of the shoulder corresponding to the [A_1(TO), E(LO)] mode at ~190 cm^{-1} by its frequency up-shift and overlapping with the downshifting [$A_1(TO_2)$] mode indicates that in the temperature range of (275 – 300) K the structure changes from O toward T. The signatures of T structure, *i.e.* the sharp character of both the "silent" mode at 299 cm^{-1} and the interference dip at 180 cm^{-1} are preserved up to 273 K. At higher temperatures

downshift and damping of the "silent" mode reveals the evolution toward the C structure. Traces of this mode, *i.e.* a residual T polar order is still detected up to 448 K. Above this temperature, the strong broadening of the Raman spectrum show a typical C phase, specific to the paraelectric state (Fig. 17(a)).

The incorporation of 5 mol. % Hf in BTH05 seems to stabilize the R structure up to 223 K. The corresponding peaks are even more prominent than those specific to the R polymorph in BT. Thus, the triple mode located at 142, 160 and 182 cm^{-1}, as well as and the related interferences dip at 152 and 175 cm^{-1} were clearly noticed. The coupling between two supplementary small peaks located at low wave numbers (105 and 115 cm^{-1}), together with the corresponding interference dip at 113 cm^{-1} are also detected in the Raman spectrum of BTH05 (see inset of Fig. 17(b)). In the mentioned insets of Figs. 17(a) and 17(b), the Raman modes of R phase are denoted by red triangular symbols, while the interferences dip are marked by dashed lines. In the temperature range of (223 − 273), the damping of the "silent" mode and the collapse of the triple mode indicates the evolution towards an O structure, identified by the small peak located at 180 cm^{-1}, assigned to the [A_1(T), E(LO)] mode. This process seems to occur at higher temperature, but in a wider temperature range than in BT. The flattening of the [A_1(T), E(LO)] peak, which is converted into a left-side asymmetrical feature of [A_1(TO)] mode indicates a gradual evolution of the O phase toward a T structure in the temperature range of (298 − 348) K. The T modification seems to be stable up to 373 K, when the interference dip located at 176 cm^{-1} is still weakly detected. Above this temperature, the broadening of all the Raman modes suggests a gradual shift toward the C structure. The vanishing of the "silent" mode [B_1, E(TO)+ (LO)] at 423 K shows that, above this temperature, the typical C phase predominates (Fig. 17(b)). It is worth to mention that the evolution towards the C phase is more rapid and its appearance occurs at a somewhat lower temperature than in BT specimen. This result is consistent with the dielectric data, taken into account the shift of the Curie temperature to lower temperature values in Hf-doped ceramic. Hence, it is normal that BTH05 sample is found in the paraelectric state at a lower temperature than the BT ceramic.

These findings are sustained by the diagram of Fig. 17(c), which shows the temperature dependence of the "silent" mode frequency for BT and BTH05. The presence of three domains of phase-overlapping, *i.e.* (R+O), (O+T) and (T + C), were noticed. Compared to BT, for BTH05 sample the (R+O) and (O+T) domains are shifted to higher temperature values and become broader, while the (T + C) domain become narrower and shifted to lower temperature. This is consistent with the opposite variation of both the low-temperature phase transition temperatures T_1 and T_2, relative to the ferroelectric-paraelectric phase transition temperature, T_C, in homovalently *B*-site substituted $BaTiO_3$ ceramics. In the diagram of Fig. 17(c) the temperature values of the three phase transitions determined from temperature dependence of the dielectric constant are marked by dashed lines inside the di-phase domains. Domains of coexistence of crystalline phases with dissimilar symmetries were also reported in homovalently *A*-site doped barium titanate, as some (Ba,Sr) TiO_3 solid solutions [51,52].

The increase of Hf content in BTH10 determines obvious structural changes. Thus, at 248 K the R phase was detected by the corresponding low-temperature features (Fig. 18(a)). The small left-side shoulder of [A_1(TO)] mode at 188 cm^{-1} suggests that the presence of a short-range O distortion cannot be excluded.

At higher temperatures the bands specific to the polar order gradually diminish, indicating the evolution toward a C phase. Traces of R distortion are still detectable up to 348 K (red triangular symbols for peaks and dashed lines for interferences dip in inset of Fig. 18(a)), while the slightly asymmetric profile of the [A_1(TO)] mode is maintained up to 398 K (inset of Fig. 18(a)). Only above this temperature any asymmetry of [A_1(TO)] band seems to disappear, the broadening of the spectra indicating the C structure specific to the paraelectric state (Fig. 18(a)).

The temperature dependence of Raman scattering in BTH20 is also very interesting. Increasing solute proportion induces the shift of [A_1(TO)], [A_1(TO), E(TO)] and [A_1(LO), E(LO)] modes to higher frequencies. The presence of the "silent" mode is not detectable even at lower temperatures, but instead, [A_1(TO)] band exhibits a right-side asymmetric profile and a significant shift to ~289 cm^{-1}. The absence of both the "silent mode" [B_1, E(TO+LO)] and the interference dip at 180 cm^{-1} in all the Raman spectra of BTH20 indicates that, regardless of the temperature, T distortion is not present in the sample. The temperature-induced flattening of Raman scattering is less obvious and the R phase is more thermally stable than in BTH10 (Fig. 18(b)). Hence, traces of polar distortions are visible even at 473 K, although at this temperature the sample should be found in the paraelectric state.

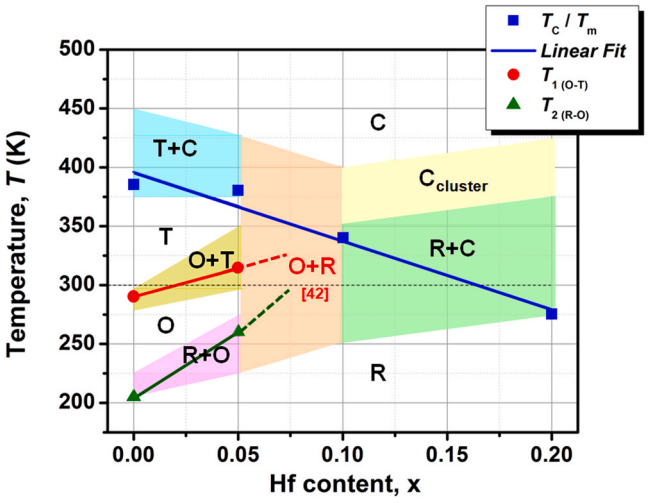

Fig. 19. Proposed phase diagram for the $BaTiO_3$ − $BaHfO_3$ system, based on both the data of low-field dielectric analysis and Raman spectroscopy results, for SP-sintered BTH ceramics derived from nanopowders synthesized by the modified Pechini method.

The difference in the evolution of Raman scattering of BTH10 and BTH20 could be explained in terms of the specific features related to the "pinched" ferroelectric-paraelectric phase transition in the two mentioned compositions. The increased Hf content in BTH20 compared to BTH10 therefore causes not only the equivalent T_m fall from 345 to 325 K, but also a more pronounced diffuseness of the phase transition, as indicated by the permittivity data *vs*. temperature. BTH10 evolves more steeply towards the paraelectric phase than BTH20, which seems to maintain a less pronounced but more stable polar order far above T_m. This finding supports the assumption that randomly distributed nano-sized polar clusters embedded in a cubic matrix as in a relaxor-like state, may occur at high temperature, prior to the development of a typical paraelectric state, which seems not to have been reached yet at the maximum temperature used for the Raman scattering investigations carried out in this study.

The diagram of Fig. 18(c) based on thermo-Raman scattering data, which presents the temperature dependence of frequency for the [A_1(TO), E(TO)] mode in BTH10 and BTH20 samples reveals in both cases a wide temperature domain in which R and C polymorphs coexist. This domain, as well as the one corresponding to the polar nanoregions, is shifted towards higher temperatures in BTH20, compared to the BTH10 sample.

The presence of di-phase domains in the fine-grained SP-sintered BTH ceramics examined in this work allowed proposing a low-temperature phase diagram of the $BaTiO_3$–$BaHfO_3$ system, based on both the thermo-Raman scattering and dielectric data (Fig. 19).

4. Conclusions

The present work is dedicated to the investigations of perovskite

$BaHf_xTi_{1-x}O_3$ (x = 0, 0.05, 0.10 and 0.20) dense ceramics consolidated by SPS method by using Pechini-derived nanopowders.

The dielectric study demonstrated a similar trend as reported in other homovalent substitutions on Ti sites of $BaTiO_3$ ceramics: the Curie temperature (T-C) reduction and the increase of the temperature of both the ferroelectric-ferroelectric polymorph transformations (R-O) and (O-T), giving rise to a pinched transition at about x = 0.10. The increasing of Hf amount results in a ferroelectric-relaxor transformation, which was confirmed by structural, dielectric and Raman analyses. The Hf addition plays an inhibiting role on the grain growth in ceramics. Due to this effect, a strong grain size reduction towards the nanometre range is noticed, in particular for BTH10 and BTH20. The local compositional inhomogeneity, the severe grain size refinement and the shift of the paraelectric state towards room temperature play a synergic role on the room temperature functional properties, giving rise to specific features, as: reduction of permittivity, of the polarization values, of hysteresis loop area and of tunability, together with a higher degree of diffuseness of the ferroelectric-paraelectric phase transition as result of the broad ranges for the dissimilarly-distorted phases superposition. Increasing Hf content and its related effect of grain size drop determines a higher thermal stability of the dielectric response and lower dielectric losses, also representing a pathway for the rise of energy storage efficiency in heavily Hf-substituted barium titanate ceramics. The low losses maintained until high values of the dc voltages, together with permittivity reduction below 1000, reasonable high tunability and lack of hysteresis make the compositions x = 0.10 and 0.20 appealing for tunability microwave applications. Furthermore, the $BaTi_{0.90}Hf_{0.10}O_3$ composition's remarkable storage efficiency (η = 87 %) makes this nanocrystalline ceramic a viable option for energy storage devices. Therefore, the grain size reduction induced by both the Hf substitution and the use of fast sintering method provide a reliable tool for approaching the conditions for tunability applications for specific compositions, as alternative to the dilution methods previously proposed.

CRediT authorship contribution statement

Pătru Roxana-Elena: Writing – original draft, Visualization, Validation, Methodology, Investigation, Formal analysis, Data curation, Conceptualization, Writing – review & editing. **Cătălina-Andreea Stanciu:** Methodology, Investigation, Formal analysis. **Elena Mirabela Soare:** Methodology, Formal analysis, Data curation, Conceptualization, Writing- original draft, Visualization, Validation, Investigation. **Ianculescu Adelina:** Writing – review & editing, Writing – original draft, Visualization, Validation, Supervision, Resources, Project administration, Methodology, Investigation, Funding acquisition, Formal analysis, Data curation, Conceptualization, Software. **Roxana Doina Truşcă:** Methodology, Investigation, Data curation. **Adrian-Ionuţ Nicoară:** Methodology, Investigation, Data curation. **Bogdan Ştefan Vasile:** Methodology, Investigation, Data curation. **Ioana Pintilie:** Methodology, Investigation, Data curation. **Liliana Mitoşeriu:** Writing – review & editing, Validation, Methodology, Investigation, Conceptualization, Visualization. **Nadejda Horchidan:** Methodology, Investigation, Data curation, Conceptualization. **Vasile-Adrian Surdu:** Methodology, Investigation, Data curation.

Declaration of Competing Interest

The authors declare that they have no known competing financial interests or personal relationships that could have appeared to influence the work reported in this paper.

Acknowledgement

The authors are grateful to Romanian Ministry of Research, Innovation and Digitization through the National Programme "Installations and Strategic Objectives of National Interest" for access to infrastructure. N.H. and L.M. acknowledge the Romanian grant PN-IV-P2–2.1-TE-2023–1488 (HARVENERGY). R.E.P and I.P acknowledge the financial support from the Core Program of the National Institute of Materials Physics 2023–2026, Project PC2–PN23080202, funded by the Romanian Ministry of Research, Innovation and Digitization.

References

[1] M.E. Lines, A.M. Glass, Principles and applications of ferroelectrics and related materials. Oxford: Clarendon, 1977.
[2] C.A. Randall, Scientific and engineering issues of the state-of-the-art and future multilayer capacitors, J. Ceram. Soc. Jpn. 109 (2001) S2–S6, https://doi.org/10.2109/jcersj.109.S2.
[3] D. Gulwade, Lead-Free Ferroelectrics: Barium Titanate Based Ceramics: Past, Present, and Future. Advances in Nanostructured Materials, Springer, 2022, pp. 359–379, https://doi.org/10.1007/978-981-16-8391-6_18.
[4] V. Kumar, I.Packia Selvam, K. Jithesh, P.V. Divya, Preparation and dielectric characteristics of nanocrystalline $Ba(M_xTi_{1-x})O_3$, J. Phys. D Appl. Phys. 40 (9) (2007) 2936–2940, https://doi.org/10.1088/0022-3727/40/9/040.
[5] V. Müller, H. Beige, H.P. Abicht, Non-Debye dielectric dispersion of barium titanate stannate in the relaxor and diffuse phase-transition state, Appl. Phys. Lett. 84 (8) (2004) 1341–1343, https://doi.org/10.1063/1.1649820.
[6] V.V. Shvartsman, K. Kleemann, J. Dec, Z.K. Xu, S.G. Lu, Diffuse phase transition in $BaTi_{1-x}Sn_xO_3$ ceramics: an intermediate state between ferroelectric and relaxor behaviour, J. Appl. Phys. 99 (12) (2006) 124111, https://doi.org/10.1063/1.2207828.
[7] X. Wei, X. Yao, Preparation, structure and dielectric property of barium stannate titanate ceramics, Mater. Sci. Eng. B 137 (1-3) (2007) 184–188, https://doi.org/10.1016/j.mseb.2006.11.012.
[8] X. Wei, Y. Feng, X. Wan, X. Yao, Evolvement of dielectric relaxation of barium stannate titanate ceramics, Ceram. Int. 30 (7) (2004) 1397–1400, https://doi.org/10.1016/j.ceramint.2003.12.088.
[9] X. Wei, Y. Feng, X. Wan, X. Yao, Dielectric properties of barium stannate titanate ceramics under bias field, Ceram. Int. 30 (7) (2004) 1401–1404, https://doi.org/10.1016/j.ceramint.2003.12.084.
[10] N. Horchidan, A.C. Ianculescu, L.P. Curecheriu, F. Tudorache, V. Musteata, S. Stoleriu, N. Drăgan, D. Crisan, S. Tascu, L. Mitoseriu, Preparation and characterization of barium titanate stannate solid solutions, J. Alloy Compd. 509 (14) (2011) 4731–4737, https://doi.org/10.1016/j.jallcom.2011.01.123.
[11] N. Horchidan, A.C. Ianculescu, C.A. Vasilescu, M. Deluca, V. Musteata, H. Ursic, R. Frunza, B. Malic, L. Mitoseriu, Multiscale study of ferroelectric-relaxor crossover in $BaSn_xTi_{1-x}O_3$ ceramics, J. Eur. Ceram. Soc. 34 (15) (2014) 3661–3674, https://doi.org/10.1016/j.jeurceramsoc.2014.06.005.
[12] M. Deluca, L. Stoleriu, L.P. Curecheriu, N. Horchidan, A.C. Ianculescu, C. Galassi, L. Mitoseriu, High-field dielectric properties and Raman spectroscopic investigation of the ferroelectric-to-relaxor crossover in $BaSn_xTi_{1-x}O_3$ ceramics, J. Appl. Phys. 111 (8) (2012) 084102, https://doi.org/10.1063/1.3703672.
[13] S. Hennings, A. Schnell, G. Simon, Diffuse ferroelectric phase transitions in $Ba(Ti_{1-y}Zr_y)O_3$ ceramics, J. Am. Ceram. Soc. 65 (11) (1982) 539–544, https://doi.org/10.1111/j.1151-2916.1982.tb10778.x.
[14] A. Simon, J. Ravez, M. Maglione, The crossover from a ferroelectric to a relaxor state in lead-free solid solutions, J. Phys. Condens. Matter 16 (6) (2004) 963–970, https://doi.org/10.1088/0953-8984/16/6/023.
[15] X.G. Tang, K.H. Chew, K.L.W. Chan, Diffuse phase transition and dielectric tunability of $Ba(Zr_yTi_{1-y})O_3$ relaxor ferroelectric ceramics, Acta Mater. 52 (17) (2004) 5177–5183, https://doi.org/10.1016/j.actamat.2004.07.028.
[16] F. Moura, A.Z. Simões, B.D. Stojanovic, M.A. Zaghete, E. Longo, J.A. Varela, Dielectric and ferroelectric characteristics of barium zirconate titanate ceramics prepared from mixed oxide method, J. Alloy Compd. 462 (1-2) (2008) 129–134, https://doi.org/10.1016/j.jallcom.2007.07.077.
[17] A. Ianculescu, L. Mitoşeriu, $Ba(Ti,Zr)O_3$ – Functional Materials: From Nanopowders to Bulk Ceramics, NovaScience Publishers Inc, Hauppauge New York, USA, 2010.
[18] A.A. Bokov, M. Maglione, A. Simon, Z.-G. Ye, Dielectric behavior of $Ba(Ti_{1-x}Zr_x)O_3$ solid solution, Ferroelectrics 337 (1) (2011) 169–178, https://doi.org/10.1080/00150190600716747.
[19] A. Chen, Y. Zhi, J. Zhi, P.M. Vilarinho, J.L. Baptista, Synthesis and characterization of Ba $(Ti_{1-x}Ce_x)O_3$ ceramics, J. Eur. Ceram. Soc. 17 (10) (1997) 1217–1221, https://doi.org/10.1016/S0955-2219(96)00220-8.
[20] C. Ang, Z. Jing, Z. Yu, Ferroelectric relaxor $Ba(Ti,Ce)O_3$, J. Phys. Condens. Matter 14 (38) (2002) 8901–8912, https://doi.org/10.1088/0953-8984/14/38/313.
[21] Z. Jing, Z. Yu, C. Ang, Crystalline structure and dielectric properties of Ba $(Ti_{1-y}Ce_y)O_3$, J. Mater. Sci. 38 (5) (2003) 1057–1061, https://doi.org/10.1023/A:1022306132064.
[22] G. Canu, G. Confalonieri, M. Deluca, L. Curecheriu, M.T. Buscaglia, M. Asandulesa, N. Horchidan, M. Dapiaggi, L. Mitoseriu, V. Buscaglia, Structure-property correlations and origin of relaxor behaviour in $BaCe_xTi_{1-x}O_3$, Acta Mater. 152 (2018) 258–268, https://doi.org/10.1016/j.actamat.2018.04.038.
[23] S. Anwar, P.R. Sagdeo, N.P. Lalla, Crossover from classical to relaxor ferroelectrics in $BaTi_{1-x}Hf_xO_3$ ceramics, J. Phys. Condens. Matter 18 (13) (2006) 3455–3468, https://doi.org/10.1088/0953-8984/18/13/013.
[24] S. Anwar, P.R. Sagdeo, N.P. Lalla, Ferroelectric relaxor behaviour in hafnium doped barium-titanate ceramic, Solid State Commun. 138 (7) (2006) 331–336, https://doi.org/10.1016/j.ssc.2006.03.018.

[25] S. Anwar, P.R. Sagdeo, N.P. Lalla, Study of the relaxor behaviour in $BaTi_{1-x}Hf_xO_3$ ($0.20 \leq x \leq 0.30$) ceramics, Solid State Sci. 9 (11) (2007) 1054–1060, https://doi.org/10.1016/j.solidstatesciences.2007.07.023.

[26] S. Anwar, P.R. Sagdeo, N.P. Lalla, Locating the normal to relaxor phase boundary in $Ba(Ti_{1-x}Hf_x)O_3$ ceramics, Mater. Res. Bull. 43 (7) (2008) 1761–1769, https://doi.org/10.1016/j.materresbull.2007.07.013.

[27] H.Y. Tian, Y. Wang, J. Miao, H.L.W. Chan, C.L. Choy, Preparation and characterization of hafnium doped barium titanate ceramics, J. Alloy Compd. 431 (1-2) (2007) 197–202, https://doi.org/10.1016/j.jallcom.2006.05.037.

[28] R.D. Shannon, Revised effective ionic radii and systematic studies of interatomic distances in halides and chalcogenides, Acta Cryst. A 32 (1976) 751–767, https://doi.org/10.1107/S0567739476001551.

[29] R. Farhi, M. El Marssi, A. Simon, J. Ravez, A Raman and dielectric study of ferroelectric $Ba(Ti_{1-x}Zr_x)O_3$ ceramics, Eur. Phys. J. B 9 (4) (1999) 599–604, https://doi.org/10.1007/s100510050803.

[30] Z. Yu, C. Ang, R. Guo, A.S. Bhalla, Piezoelectric and strain properties of $BaTi_{1-x}Zr_xO_3$ ceramics, J. Appl. Phys. 92 (3) (2002) 1489–1493, https://doi.org/10.1063/1.1487435.

[31] G. Tang, J. Wang, X.X. Wang, H.L.W. Chan, Effects of grain size on the dielectric properties and tunabilities of sol-gel derived $Ba(Zr_{0.2}Ti_{0.8})O_3$ ceramics, Solid State Commun. 131 (3-4) (2004) 163–168, https://doi.org/10.1016/j.ssc.2004.05.016.

[32] W. Cai, C. Fu, J. Gao, H. Chen, Effects of grain size on domain structure and ferroelectric properties of barium zirconate titanate ceramics, J. Alloy Compd. 480 (2) (2009) 870–873, https://doi.org/10.1016/j.jallcom.2009.02.049.

[33] M. Deluca, C.A. Vasilescu, A.C. Ianculescu, D.C. Berger, C.E. Ciomaga, L. P. Curecheriu, L. Stoleriu, A. Gajovic, L. Mitoseriu, C. Galassi, Investigation of the composition-dependent properties of $BaTi_{1-x}Zr_xO_3$ ceramics prepared by the modified Pechini method, J. Eur. Ceram. Soc. 32 (13) (2012) 3551–3566, https://doi.org/10.1016/j.jeurceramsoc.2012.05.007.

[34] C.E. Ciomaga, M. Viviani, M.T. Buscaglia, V. Buscaglia, L. Mitoşeriu, A. Stancu, P. Nanni, Preparation and characterisation of the $Ba(Zr,Ti)O_3$ ceramics with relaxor properties, J. Eur. Ceram. Soc. 27 (13-15) (2007) 4061–4604, https://doi.org/10.1016/j.jeurceramsoc.2007.02.095.

[35] W.H. Payne, V.J. Tennery, Dielectric and structural investigations of the system $BaTiO_3$-$BaHfO_3$, J. Am. Ceram. Soc. 48 (8) (1965) 413–417, https://doi.org/10.1111/j.1151-2916.1965.tb14779.x.

[36] S.K. Das, B.K. Roul, Double hysteresis loop in $BaTi_{1-x}Hf_xO_3$ ferroelectric ceramics, J. Mater. Sci Mater. Electron 26 (8) (2015) 5833–5838, https://doi.org/10.1007/s10854-015-3143-8.

[37] B. Garbarz-Glos, W. Bak, A. Molak, A. Kalvane, Microstructure, calorimetric and dielectric investigation of hafnium doped barium titanate ceramics, Phase Transit 86 (9) (2013) 917–925, https://doi.org/10.1080/01411594.2012.745538.

[38] J. Li, D. Zhang, S. Qin, T. Li, M. Wu, D. Wang, Y. Bai, X. Lou, Large room-temperature electrocaloric effect in lead-free $BaHf_xTi_{1-x}O_3$ ceramics under low electric field, Acta Mater. 115 (2016) 58–67, https://doi.org/10.1016/j.actamat.2016.05.044.

[39] M.-D. Li, X.-G. Tang, S.-M. Zeng, Q.-X. Liu, Y.-P. Jiang, T.-F. Zhang, W.-H. Li, Large electrocaloric effect in lead-free $Ba(Hf_xTi_{1-x})O_3$ ferroelectric ceramics for clean energy applications, ACS Sustain. Chem. Eng. 6 (7) (2018) 8920–8925, https://doi.org/10.1021/acssuschemeng.8b01277.

[40] M.-D. Li, X.-G. Tang, S.-M. Zeng, Q.-X. Liu, Y.-P. Jiang, T.-F. Zhang, W.-H. Li, Phase structure analysis and pyroelectric energy harvesting performance of $Ba(Hf_xTi_{1-x})O_3$ ceramics, J. Am. Ceram. Soc. 102 (6) (2019) 3623–3629, https://doi.org/10.1111/jace.16237.

[41] H.-M. Yin, W.-J. Xu, H.-W. Zhou, X.-Y. Zhao, Y.-N. Huang, Effects of phase composition and grain size on the piezoelectric properties of HfO_2-doped barium titanate ceramics, J. Mater. Sci. 54 (19) (2019) 12392–12400, https://doi.org/10.1007/s10853-019-03726-y.

[42] P. Elorika, Sh Anwar, S. Anwar, Impact of synthesis-induced disorder on the structural, electrical, and optical properties of $BaTi_{1-x}Hf_xO_3$, $0 \leq x \leq 0.08$, Mater. Res. Bull. 167 (2023) 112424, https://doi.org/10.1016/j.materresbull.2023.112424.

[43] J. Fernandez, B. Bindhu, M. Prabu, K.Y. Sandhya, Effects of hafnium on the structural, optical and ferroelectric properties of sol-gel synthesized barium titanate ceramics, J. Korean Ceram. Soc. 59 (2022) 240–251, https://doi.org/10.1007/s43207-021-00170-0.

[44] V. Buscaglia, C.A. Randall, Size and scaling effects in barium titanate. An overview, J. Eur. Ceram. Soc. 40 (2020) 3744–3758, https://doi.org/10.1016/j.jeurceramsoc.2020.01.021.

[45] A.K. Tagantsev, V.O. Sherman, K.F. Astafiev, J. Venkatesh, N. Setter, Ferroelectric materials for microwave tunable applications, J. Electroceram 11 (1-2) (2003) 5–66, https://doi.org/10.1023/B:JECR.0000015661.81386.e6.

[46] J.F. Ihlefeld, D.T. Harris, R. Keech, J.L. Jones, J. Maria, S. Trolier-McKinstry, Scaling effects in perovskite ferroelectrics: fundamental limits and process-structure-property relations, J. Am. Ceram. Soc. 99 (2016) 2537–2557, https://doi.org/10.1111/jace.14387.

[47] L. Mitoseriu, L.P. Curecheriu, Nanostructured Barium Titanate Ceramics: Intrinsic versus Extrinsic Size Effects, in: M. Algueró, J.M. Gregg, L. Mitoseriu (Eds.), Nanoscale Ferroelectrics and Multiferroics, John Wiley & Sons, Ltd, Chichester, UK, 2016, pp. 473–511, https://doi.org/10.1002/9781118935743.ch15.

[48] Z. Zhao, V. Buscaglia, M. Viviani, M.T. Buscaglia, L. Mitoseriu, A. Testino, M. Nygren, M. Johnsson, P. Nanni, Grain-size effects on the ferroelectric behavior of dense nanocrystalline $BaTiO_3$ ceramics, Phys. Rev. B. 70 (2004) 024107, https://doi.org/10.1103/PhysRevB.70.024107.

[49] L. Curecheriu, S.-B. Balmus, M.T. Buscaglia, V. Buscaglia, A. Ianculescu, L. Mitoseriu, Grain size-dependent properties of dense nanocrystalline barium titanate ceramics, J. Am. Ceram. Soc. 95 (2012) 3912–3921, https://doi.org/10.1111/j.1551-2916.2012.05409.x.

[50] M.T. Buscaglia, M. Viviani, V. Buscaglia, L. Mitoseriu, A. Testino, P. Nanni, Z. Zhao, M. Nygren, C. Harnagea, D. Piazza, C. Galassi, High dielectric constant and frozen macroscopic polarization in dense nanocrystalline $BaTiO_3$ ceramics, Phys. Rev. B 73 (2006) 064114, https://doi.org/10.1103/PhysRevB.73.064114.

[51] R.E. Pătru, C.A. Stanciu, V.A. Surdu, E.M. Soare, R.D. Truşcă, B.S. Vasile, A. I. Nicoară, L. Trupină, I. Pasuk, M. Botea, N. Horchidan, L. Mitoşeriu, L. Pintilie, I. Pintilie, A.C. Ianculescu, Downscaling grain size toward the nanometre range – a key-factor for tuning the crystalline structure, phase transitions, dielectric and ferroelectric behaviour in $Ba_{0.8}Sr_{0.2}TiO_3$ ceramics, Prog. Solid State Chem. 74 (2024) 100457, https://doi.org/10.1016/j.progsolidstchem.2024.100457.

[52] R.E. Pătru, C.A. Stanciu, E.M. Soare, V.A. Surdu, R.D. Truşcă, A.I. Nicoară, B. S. Vasile, G. Boni, L. Amarande, N. Horchidan, L.P. Curecheriu, L. Mitoşeriu, L. Pintilie, I. Pintilie, A.C. Ianculescu, Grain size-driven effect on the functional properties in $Ba_{0.6}Sr_{0.4}TiO_3$ ceramics consolidated by spark plasma sintering, J. Eur. Ceram. Soc. 43 (2023) 3250–3265, https://doi.org/10.1016/j.jeurceramsoc.2023.02.013.

[53] V.L. Ene, V.R. Lupu, C.V. Condor, R.E. Patru, L.M. Hrib, L. Amarande, A.I. Nicoara, L. Pintilie, A.C. Ianculescu, Influence of Grain Size on Dielectric Behavior in Lead-Free $0.5Ba(Zr_{0.2}Ti_{0.8})O_3$–$0.5(Ba_{0.7}Ca_{0.3})TiO_3$ Ceramics, Nanomaterials 13 (2023) 2934, https://doi.org/10.3390/nano13222934.

[54] V.A. Surdu, M.A. Marinică, R.E. Pătru, O.C. Oprea, A.I. Nicoară, B.S. Vasile, R. Truşcă, A.C. Ianculescu, High-entropy lead-free perovskite $Bi_{0.2}K_{0.2}Ba_{0.2}Sr_{0.2}Ca_{0.2}TiO_3$ powders and related ceramics: synthesis, processing, and electrical properties, Nanomaterials 13 (2023) 2974, https://doi.org/10.3390/nano13222974.

[55] B. Li, X. Wang, M. Cao, L. Hao, Densification of uniformly small-grained $BaTiO_3$ using spark-plasma-sintering, Mater. Chem. Phys. 82 (1) (2003) 173–180, https://doi.org/10.1016/S0254-0584(03)00195-0.

[56] B. Li, X. Wang, L. Li, H. Zhou, X. Liu, X. Han, Y. Zhang, X. Qi, X. Deng, Dielectric properties of fine-grained $BaTiO_3$ prepared by spark-plasma-sintering, Mater. Chem. Phys. 83 (1) (2004) 23–28, https://doi.org/10.1016/j.matchemphys.2003.08.009.

[57] A. Ianculescu, L. Mitoseriu, D. Berger, C.E. Ciomaga, D. Piazza, C. Galassi, Composition dependent ferroelectric properties of $Ba_{1-x}Sr_xTiO_3$ ceramics, Phase Transit 79 (6-7) (2006) 375–388, https://doi.org/10.1080/01411590600892062.

[58] A. Ianculescu, D. Berger, M. Viviani, C. Ciomaga, L. Mitoseriu, E. Vasile, N. Drăgan, D. Crişan, Investigation of $Ba_{1-x}Sr_xTiO_3$ ceramics prepared from powders synthesized by the modified Pechini route, J. Eur. Ceram. Soc. 27 (13-15) (2007) 3655–3658, https://doi.org/10.1016/j.jeurceramsoc.2007.02.017.

[59] A. Ianculescu, D. Berger, L. Mitoşeriu, L.P. Curecheriu, N. Drăgan, D. Crişan, E. Vasile, Properties of $Ba_{1-x}Sr_xTiO_3$ ceramics prepared by the modified-Pechini method, Ferroelectrics 369 (1) (2008) 22–34, https://doi.org/10.1080/00150190802371424.

[60] F.M. Tufescu, L. Curecheriu, A. Ianculescu, C.E. Ciomaga, L. Mitoseriu, High-voltage tunability measurements of the $BaZr_xTi_{1-x}O_3$ ferroelectric ceramics, J. Optoelectron. Adv. M. 10 (7) (2008) 1894–1897.

[61] T. Takeuchi, K. Ado, T. Asai, H. Kageyama, Y. Saito, C. Masquelier, O. Nakamura, Thickness of cubic surface phase on barium titanate single-crystalline grains, J. Am. Ceram. Soc. 77 (6) (1994) 1665–1668, https://doi.org/10.1111/j.1151-2916.1994.tb09774.x.

[62] M.B. Smith, K. Page, Th Siegrist, P.L. Redmond, E.C. Walter, R. Seshadri, L.E. Brus, M.L. Steigerwald, Crystal structure and the paraelectric-to-ferroelectric phase transition of nanoscale $BaTiO_3$, J. Am. Chem. Soc. 130 (22) (2008) 6955–6963, https://doi.org/10.1021/ja0758436.

[63] V. Petkov, V. Buscaglia, M.T. Buscaglia, Z. Zhao, Y. Ren, Structural coherence and ferroelectricity decay in submicron- and nano-sized perovskites, Phys. Rev. B 78 (5) (2008) 054107, https://doi.org/10.1103/PhysRevB.78.054107.

[64] K. Page, T. Proffen, M. Niederberger, R. Seshadri, Probing local dipoles and ligand structure in $BaTiO_3$ nanoparticles, Chem. Mater. 22 (15) (2010) 4386–4391, https://doi.org/10.1021/cm100440p.

[65] Y. Gao, V.V. Shvartsman, D. Gautam, M. Winterer, D.C. Lupascu, Nanocrystalline barium strontium titanate ceramics synthesized via the "Organosol" route and spark plasma sintering, J. Am. Ceram. Soc. 97 (7) (2014) 2139–2146, https://doi.org/10.1111/jace.12933.

[66] M. Botea, I. Pintilie, V.-A. Surdu, C.-A. Stanciu, R.-D. Truşcă, B.S. Vasile, R. Patru, A.-C. Ianculescu, L. Pintilie, Structural, functional properties and enhanced thermal stability of bulk graded $(Ba,Sr)TiO_3$ structures obtained by spark plasma sintering, J. Mater. Res. Technol. 12 (2021) 2085–2103, https://doi.org/10.1016/j.jmrt.2021.06.001.

[67] A.K. Kalyani, K. Brajesh, A. Senyshyn, R. Ranjan, Orthorhombic-tetragonal phase coexistence and enhanced piezo-response at room temperature in Zr, Sn, and Hf modified $BaTiO_3$, Appl. Phys. Lett. 104 (2014) 252906, https://doi.org/10.1063/1.4885516.

[68] A.K. Kalyani, R. Ranjan, Anomalous piezoelectric response due to stabilization of two ferroelectric phases in Zr-modified $BaTiO_3$, J. Phys. Condens. Matter 25 (2013) 362203, https://doi.org/10.1088/0953-8984/25/36/362203.

[69] Y. Avrahami, H.L. Tuller, Improved electromechanical response in rhombohedral $BaTiO_3$, J. Electroceram 13 (1-3) (2004) 463–469, https://doi.org/10.1007/s10832-004-5143-6.

[70] L.E. Cross, Relaxor, Ferroelectr. Overv. Ferroelectr. 151 (1994) 305–320, https://doi.org/10.1080/00150199408244755.

[71] K. Uchino, S. Nomura, Critical exponents of the dielectric constants in diffused-phase-transition crystals, Ferroelectr. – Lett. Sect. 44 (1) (1982) 55–61, https://doi.org/10.1080/00150198208260644.

[72] K. Funke, Jump relaxation in solid electrolytes, Prog. Solid State Chem. 22 (2) (1993) 111–195, https://doi.org/10.1016/0079-6786(93)90002-9.
[73] Z. Li, H. Fan, Polaron relaxation associated with the localized oxygen vacancies in $Ba_{0.85}Sr_{0.15}TiO_3$ ceramics at high temperatures, J. Appl. Phys. 106 (2009) 054102, https://doi.org/10.1063/1.3211308.
[74] S. Havriliak, S.A. Negami, Complex plane representation of dielectric and mechanical relaxation processes in some polymers, Polymer 8 (1967) 161–210, https://doi.org/10.1016/0032-3861(67)90021-3.
[75] A.K. Jonscher, Dielectric Relaxation in Solids, Chelsea Dielectrics Press, London, UK, 1983.
[76] E. Kröll, L. Devecioglu, A.N. Salak, L. Piotrowsky, V.V. Shvartsman, D.C. Lupascu, Weakly-coupled barium titanate stannate-based relaxors as energy storage materials (in press), J. Am. Ceram. Soc. (2025) e20413, https://doi.org/10.1111/jace.20413.
[77] R.E. Stanculescu, N. Horchidan, C. Galassi, M. Asandulesa, L. Padurariu, C. E. Ciomaga, L. Mitoseriu, Porous (Ba, Sr)TiO_3 ceramics for tailoring dielectric and tunability properties: modelling and experiment, Process. Appl. Ceram. 11 (4) (2017) 235–246, https://doi.org/10.2298/PAC1704235S.
[78] U.-C. Chung, C. Elissalde, M. Maglione, Low-losses, highly tunable $Ba_{0.6}Sr_{0.4}TiO_3$/MgO composite, Appl. Phys. Lett. 92 (2008) 042902, https://doi.org/10.1063/1.2837621.
[79] A. Scalabrin, A.S. Chaves, D.S. Shim, S.P.S. Porto, Temperature dependence of the A_1 and E optical phonons in $BaTiO_3$, Phys. Stat. Sol. (b) 79 (1977) 731–742, https://doi.org/10.1002/pssb.2220790240.
[80] A. Chaves, R.S. Katiyar, S.P.S. Porto, Coupled modes with A_1, symmetry in tetragonal $BaTiO_3$, Phys. Rev. B 10 (8) (1974) 3522–3533, https://doi.org/10.1103/PhysRevB.10.3522.
[81] M. DiDomenico, S.H. Wemple, S.P.S. Porto, R.P. Bauman, Raman Spectrum of Single-Domain $BaTiO_3$, Phys. Rev. 174 (1968) 522–530, https://doi.org/10.1103/PhysRev.174.522.
[82] Y.-J. Jiang, L.-Z. Zeng, R.-P. Wang, Fundamental and second-order Raman Spectra of $BaTiO_3$, J. Raman Spectrosc. 27 (1996) 31–34, https://doi.org/10.1002/(SICI)1097-4555(199601)27:1<31::AID-JRS920>3.0.CO;2-K.
[83] J.Q. Qi, T. Peng, Y.M. Hu, L. Sun, Y. Wang, W.P. Chen, L.T. Li, C.W. Nan, H.L. W. Chan, Direct Synthesis of ultrafine tetragonal $BaTiO_3$ nanoparticles at room temperature, Nanoscale Res. Lett. 6 (2011) 466. ⟨http://www.nanoscalereslett.com/content/6/1/466⟩.
[84] A. Sati, V. Mishra, A. Kumar, M.K. Warshi, A. Sagdeo, R. Kumar, P.R. Sagdeo, Effect of structural disorder on the electronic and phononic properties of Hf doped $BaTiO_3$, J. Mater. Sci. Mater. Electron 30 (2019) 9498–9506, https://doi.org/10.1007/s10854-019-01281-5.
[85] O.V. Rambadey, A. Kumar, A. Sati, P.R. Sagdeo, Exploring the interrelation between urbach energy and dielectric constant in Hf-substituted $BaTiO_3$, ACS Omega 6 (47) (2021) 32231–32238, https://doi.org/10.1021/acsomega.1c05057.
[86] A. Bencan, E. Oveisi, S. Hashemizadeh, V.K. Veerapandiyan, T. Hoshina, T. Rojac, M. Deluca, G. Drazic, D. Damjanovic, Atomic scale symmetry and polar nanoclusters in the paraelectric phase of ferroelectric materials, Nat. Commun. 12 (2021) 3509, https://doi.org/10.1038/s41467-021-23600-3.
[87] J. Pokorný, U.M. Pasha, L. Ben, O.P. Thakur, D.C. Sinclair, I.M. Reaney, Use of Raman spectroscopy to determine the site occupancy of dopants in $BaTiO_3$, J. Appl. Phys. 109 (2011) 114110, https://doi.org/10.1063/1.3592192.
[88] K.V. Veerapandiyan, S.H. Khosravi, G. Canu, A. Feteira, V. Buscaglia, K. Reichmann, M. Deluca, B-site vacancy induced Raman scattering in $BaTiO_3$-based ferroelectric ceramics, J. Eur. Ceram. Soc. 40 (2020) 4684–4688, https://doi.org/10.1016/j.jeurceramsoc.2020.05.051.
[89] N. Binhayeeniyi, P. Sukvisut, C. Thanachayanont, S. Muensit, Physical and electromechanical properties of barium zirconium titanate synthesized at low-sintering temperature, Mater. Lett. 64 (2010) 305–308, https://doi.org/10.1016/j.matlet.2009.10.069.
[90] X. Jiang, H. Hao, Y. Yang, E. Zhou, S. Zhang, P. Wei, M. Cao, Z. Yao, H. Liu, Structure and enhanced dielectric temperature stability of $BaTiO_3$-based ceramics by Ca ion B site-doping, J. Mater. 7 (2) (2020) 295–301, https://doi.org/10.1016/j.jmat.2020.09.001.
[91] M.H. Frey, D.A. Payne, Grain-size effect on structure and phase transformations for barium titanate, Phys. Rev. B. 54 (1996) 3158–3168, https://doi.org/10.1103/PhysRevB.54.3158.
[92] T. Takeuchi, C. Capiglia, N. Balakrishnan, Y. Takeda, H. Kageyama, Preparation of fine-grained $BaTiO_3$ ceramics by spark plasma sintering, J. Mater. Res. 17 (2002) 575–581, https://doi.org/10.1557/JMR.2002.0081.
[93] R. Farhi, M. El Marssi, A. Simon, J. Ravez, A Raman and dielectric study of ferroelectric $Ba(Ti_{1-x}Zr_x)O$ ceramics, Eur. Phys. J. B 9 (4) (1999) 599–604.
[94] S. Miao, J. Pokorný, U.M. Pasha, O.P. Thakur, D.C. Sinclair, I.M. Reaney, Polar order and diffuse scatter in $Ba(Ti_{1-x}Zr_x)O_3$ ceramics, J. Appl. Phys. 106 (11) (2009) 114111, https://doi.org/10.1063/1.3253735.
[95] A. Sati, P. Pokhriyal, A. Kumar, S. Anwar, A. Sagdeo, N.P. Lalla, P.R. Sagdeo, Origin of ferroelectricity in cubic phase of Hf substituted $BaTiO_3$, J. Phys. Condens. Matter 33 (2021) 1–14, https://doi.org/10.1088/1361-648X/abf0bf.
[96] C.H. Perry, D.B. Hall, Temperature dependence of the Raman spectrum of $BaTiO_3$, Phys. Rev. Lett. 15 (17) (1965) 700–702, https://doi.org/10.1103/PhysRevLett.15.700.